Methyl, ethyl, and propyl nitrates: global distribution and impacts on reactive nitrogen in remote marine environments

Jenny A. Fisher[1,2], Elliot L. Atlas[3], Barbara Barletta[4], Simone Meinardi[4], Donald R. Blake[4], Chelsea R. Thompson[5,6], Thomas B. Ryerson[6], Jeff Peischl[5,6], Zitely A. Tzompa-Sosa[7], Lee T. Murray[8]

[1]Centre for Atmospheric Chemistry, School of Chemistry, University of Wollongong, Wollongong, New South Wales, Australia.
[2]School of Earth and Environmental Sciences, University of Wollongong, Wollongong, New South Wales, Australia.
[3]Department of Atmospheric Sciences, Rosenstiel School of Marine and Atmospheric Sciences, University of Miami, Miami, Florida, USA.
[4]Department of Chemistry, University of California,Irvine, Irvine, California, USA.
[5]Cooperative Institute for Research in Environmental Sciences, University of Colorado, Boulder, Colorado, USA.
[6]Chemical Sciences Division, NOAA Earth System Research Laboratory, Boulder, Colorado, USA.
[7]Department of Atmospheric Science, Colorado State University, Fort Collins, Colorado, USA.
[8]Department of Earth and Environmental Sciences, University of Rochester, Rochester, New York, USA.

Key Points:

- Model including air-sea exchange reproduces observed alkyl nitrates from 20 years of aircraft data
- Methyl nitrate is the dominant form of reactive nitrogen in the tropical Pacific and Southern Ocean
- Alkyl nitrates serve as a small but growing source of nitrogen oxides to the remote troposphere

Corresponding author: Jenny A. Fisher, jennyf@uow.edu.au

Abstract

Alkyl nitrates ($RONO_2$) are important components of tropospheric reactive nitrogen that serve as reservoirs for nitrogen oxides ($NO_x \equiv NO + NO_2$). Here we implement a new simulation of methyl, ethyl, and propyl nitrates in a global chemical transport model (GEOS-Chem). We show that the model can reproduce the spatial and seasonal variability seen in a 20-year ensemble of airborne observations. Methyl nitrate accounts for 17 Gg N globally, with maxima over the tropical Pacific and Southern Ocean. Propyl nitrate is enhanced in continental boundary layers, but its global impact (6 Gg N) is limited by a short lifetime (8 days, versus 26 days for methyl nitrate and 14 days for ethyl nitrate) that inhibits long-range transport. Ethyl nitrate has the smallest impact of the three species (4 Gg N). We find that methyl nitrate is the dominant form of reactive nitrogen (NO_y) in the Southern Ocean marine boundary layer, where its addition to the model corrects a large NO_y underestimate in austral winter relative to recent aircraft data. Combined, $RONO_2$ serve as a small net NO_x source to the marine troposphere, except in the northern mid-latitudes where the continental outflow is enriched in precursors that promote in situ $RONO_2$ formation. Recent growth in NO_x emissions from East Asia has enhanced the role of $RONO_2$ as a source of NO_x to the remote free troposphere. This relationship implies projected future emissions growth across the southern hemisphere may further enhance the importance of $RONO_2$ as a NO_x reservoir.

1 Introduction

Nitrogen oxides ($NO_x \equiv NO + NO_2$) are precursors to tropospheric ozone production, contribute to inorganic and organic aerosol formation, and enhance nitrogen deposition to ecosystems. Atmospheric NO_x has a short lifetime but can be sequestered via formation of longer-lived reactive nitrogen reservoir species including peroxy acetyl nitrate (PAN) and alkyl nitrates ($RONO_2$). In remote environments where primary NO_x emissions are limited, degradation of these nitrogen reservoirs serves as the dominant NO_x source. While NO_x production from PAN requires warm temperatures and is most significant in subsiding polluted air masses [*Singh*, 1987; *Hudman et al.*, 2004; *Zhang et al.*, 2008], the source from $RONO_2$ is primarily due to photolysis [*Clemitshaw et al.*, 1997; *Talukdar et al.*, 1997] and is therefore more diffuse. In this work, we focus exclusively on short-chain (C_1–C_3) $RONO_2$, which have lifetimes that are sufficiently long to allow long-range transport from source regions. Short-chain $RONO_2$ species have both con-

tinental [*Roberts et al.*, 1996; *Perring et al.*, 2010; *Farmer et al.*, 2011] and marine [*Chuck*, 2002; *Dahl et al.*, 2005] sources and have been observed in diverse environments across the globe [*Atlas et al.*, 1993; *Blake et al.*, 1999; *Talbot et al.*, 2000; *Blake et al.*, 2003]. These $RONO_2$ species may therefore provide a potentially significant NO_x source to regions of the remote troposphere where PAN decomposition is limited. Here, we use airborne observations collected during 19 aircraft campaigns over a 20-year period as constraints to develop a new simulation of methyl, ethyl, and propyl $RONO_2$ in a chemical transport model (GEOS-Chem), then use the model to quantify their global distribution and the implications for reactive nitrogen in remote marine regions.

Alkyl nitrate formation in the atmosphere begins with oxidation of a parent volatile organic compound (VOC, denoted RH in reaction 1)—here methane (CH_4), ethane (C_2H_6), or propane (C_3H_8)—by the hydroxyl radical (OH) in the presence of oxygen to form a peroxy radical ($RO_2^{\cdot}$):

$$RH + OH \rightarrow R^{\cdot} + H_2O \quad (1)$$

$$R^{\cdot} + O_2 \rightarrow RO_2^{\cdot} \quad (2)$$

In the presence of NO_x, the RO_2 radical reacts with NO to either convert NO to NO_2 (R3, the dominant pathway) or form an alkyl nitrate (R4):

$$RO_2^{\cdot} + NO \rightarrow RO^{\cdot} + NO_2 \quad (3)$$

$$RO_2^{\cdot} + NO \rightarrow RONO_2 \quad (4)$$

In highly polluted urban environments, methyl nitrate can also be formed via $RO^{\cdot}$ + NO_2, but this source is thought to be insignificant on the global scale [*Flocke et al.*, 1998]. The branching ratio between reactions 4 and 3, referred to as α, represents the yield of $RONO_2$. For the species considered here, α increases from <1% for methyl nitrate (CH_3ONO_2) [*Flocke et al.*, 1998] to ≈2% for ethyl nitrate ($C_2H_5ONO_2$) [*Ranschaert et al.*, 2000] to >3% for propyl nitrate ($C_3H_7ONO_2$) [*Atkinson et al.*, 1982] — although precise measurement of α remains an important source of uncertainty in atmospheric $RONO_2$ budgets [*Butkovskaya et al.*, 2009, 2012; *Williams et al.*, 2014; *Khan et al.*, 2015; *Nault et al.*, 2016]. While reaction 3 has no net impact on available atmospheric NO_x, reaction 4 can either recycle NO_x, temporarily sequester NO_x, or permanently remove NO_x

from the atmosphere, depending on the lifetime and fate of the $RONO_2$ produced [*Perring et al.*, 2013; *Fisher et al.*, 2016]. Short-chain $RONO_2$ are removed primarily by photolysis followed by OH-initiated oxidation [*Clemitshaw et al.*, 1997; *Talukdar et al.*, 1997] — both of which return NO_2 to the atmospheric NO_x pool.

In addition to chemical formation, short-chain $RONO_2$ are also thought to be emitted directly from seawater [*Atlas et al.*, 1993; *Blake et al.*, 1999; *Talbot et al.*, 2000; *Chuck*, 2002; *Blake et al.*, 2003; *Dahl et al.*, 2005]. Ocean emission is expected to be an especially significant source of methyl nitrate [*Neu et al.*, 2008], given the low methyl nitrate yield from in situ photochemical formation [*Flocke et al.*, 1998]. In-situ $RONO_2$ production in seawater can occur via photochemical [*Dahl et al.*, 2007; *Dahl and Saltzman*, 2008] and biological [*Kim et al.*, 2015a] processes, leading to supersaturation that drives a net $RONO_2$ flux from the ocean to the atmosphere [*Chuck*, 2002; *Dahl et al.*, 2005]. Although this flux has not been measured directly, it is consistent with observations showing elevated $RONO_2$ in surface waters [*Chuck*, 2002; *Dahl et al.*, 2005; *Hughes et al.*, 2008] and in the marine boundary layer [*Atlas et al.*, 1993; *Jones et al.*, 1999; *Talbot et al.*, 2000; *Blake et al.*, 2003] over the tropics and the South Pacific.

To date, there has been only one attempt to construct a distribution of the ocean $RONO_2$ flux for use in global models. Using aircraft observations from the PEM-Tropics campaigns, *Neu et al.* [2008] inferred a constant ocean flux of 0.35 Tg N yr^{-1}, mainly from the tropical Pacific with a small contribution from the Southern Ocean. However, the model used in their study did not include atmospheric production of $RONO_2$ via reactions 1-4, which likely exaggerated the size of the ocean source [*Williams et al.*, 2014]. The *Neu et al.* [2008] estimate was also hampered by the limitations of the aircraft data available at the time, including a lack of seasonal information and particularly large uncertainties for the Southern Ocean, where only one flight leg crossed south of 45°S. Despite these limitations, this estimate is the only one to have been used in global modelling studies of $RONO_2$ and their impacts.

Over the past two decades, a large global dataset of airborne C_1–C_3 $RONO_2$ observations has been amassed, spanning a diverse range of environments, latitudes, and seasons (Table 1). Although observations suggest that short-chain $RONO_2$ may be the dominant form of reactive nitrogen in remote marine environments [*Jones et al.*, 1999; *Talbot et al.*, 2000], many models ignore these species completely. The few global mod-

els that have attempted to simulate short-chain $RONO_2$ struggle to reproduce the ensemble of observations using a single set of model assumptions [*Williams et al.*, 2014; *Khan et al.*, 2015], with uncertainty in the ocean source a large contributor [*Williams et al.*, 2014]. For example, two global models both using the top-down ocean flux derived by *Neu et al.* [2008] show estimates of the ocean contribution to the total methyl nitrate burden that range from as little as 13% [*Khan et al.*, 2015] to as much as 68% [*Williams et al.*, 2014].

Here, we develop a new simulation for C_1–C_3 $RONO_2$ in the global GEOS-Chem chemical transport model, which has been widely used for studies of reactive nitrogen [*Walker et al.*, 2010; *Paulot et al.*, 2013; *Fischer et al.*, 2014; *Geddes and Martin*, 2017] and ozone budgets [e.g., *Wu et al.*, 2007; *Zhang et al.*, 2010; *Hu et al.*, 2017] but has previously neglected these smaller alkyl nitrates. Our model includes a new, bottom-up estimate of ocean $RONO_2$ emissions that is independent of the top-down estimate from *Neu et al.* [2008] used in previous models (section 2). We exploit the 20-year ensemble of global airborne data to evaluate the model. Of particular value are the recent HIPPO and ATom observations that span the entire Pacific Ocean over a range of seasons. After showing that the new simulation can reproduce the general features of the observations (section 3), we use it to evaluate the impact of short-chain $RONO_2$ on global distributions of reactive nitrogen and ozone (section 4). We then quantify the role of exported $RONO_2$ formed near major NO_x source regions on the NO_x budget in remote regions (section 5). Finally, we test the sensitivity of our results to recent changes in the global distribution of NO_x and VOC emissions (section 6).

2 Model Description

We use as base model a modified version of GEOS-Chem v9-02 with updates that have been described in detail by *Kim et al.* [2015b], *Fisher et al.* [2016], *Travis et al.* [2016], and *Marais et al.* [2016]. *Fisher et al.* [2016] made a number of improvements to simulation of $\geq C_4$ $RONO_2$, but did not include C_1–C_3 $RONO_2$ which are added here for the first time. We simulate 2013 (plus a 2-month spin-up) driven by assimilated meteorology from the Global Monitoring and Assimilation Office Goddard Earth Observing System (GEOS-FP) product. The native $0.25^\circ \times 0.3125^\circ$ resolution of GEOS-FP is downgraded to $2^\circ \times 2.5^\circ$ for the global simulation used here. Sensitivity simulations described below use the coarser $4^\circ \times 5^\circ$ resolution for expediency, and we find there are no ma-

141 **Table 1.** Aircraft campaigns used to evaluate the GEOS-Chem short-chain alkyl nitrate simu-
142 lation, ordered by month.

Campaign	Month	Year	Region	Regional Bounds[a]
HIPPO-1[b]	Jan	2009	Pacific	70°S-60°N, 150°E-100°W[c]
ORCAS	Jan-Feb	2016	Southern Ocean	75°S-55°S, 91°W-52°W
ATOM-2	Feb	2017	Pacific	70°S-60°N, 180°W-130°W[d]
			Atlantic	70°S-60°N, 60°W-0°E[e]
TOPSE	Feb-May	2000	North American Arctic	60°N-90°N, 104°W-54°W
HIPPO-3[b]	Mar-Apr	2010	Pacific	70°S-60°N, 150°E-100°W[c]
TRACE-P	Mar-Apr	2001	North Pacific	12°N-46°N, 120°E-120°W
PEM-Tropics B	Mar-Apr	1999	Tropical Pacific	35°S-35°N, 155°E-90°W
ARCTAS-A	Apr	2008	North American Arctic	60°N-90°N, 175°W-50°W
INTEX-B	Apr-May	2006	North Pacific	19°N-60°N, 175°E-105°W[f]
ITCT-2K2	Apr-May	2002	North Pacific	26°N-48°N, 130°W-90°W
DC3	May-Jun	2012	Continental US	30°N-42°N, 105°W-80°W
HIPPO-4[b]	Jun-Jul	2010	Pacific	70°S-60°N, 150°E-100°W[c]
FRAPPE	Jul-Aug	2014	Continental US	37°N-42°N, 110°W-100°W
ATOM-1	Aug	2016	Pacific	70°S-60°N, 180°W-130°W[d]
			Atlantic	70°S-60°N, 60°W-0°E[e]
SEAC4RS	Aug-Sep	2013	Continental US	19°N-55°N, 130°W-75°W
HIPPO-5[b]	Aug-Sep	2011	Pacific	70°S-60°N, 150°E-100°W[c]
TEXAQS	Sep-Oct	2006	Continental US	28°N-35°N, 100°W-93°W
PEM-Tropics A	Sep-Oct	1996	Pacific	70°S-35°N, 150°E-125°W[f]
HIPPO-2[b]	Oct-Nov	2009	Pacific	70°S-60°N, 150°E-100°W[c]

[a]Latitude and longitude bounds of each campaign used to create the model vertical profiles shown in Figures S2, S3, and S4. For all other comparisons, all available aircraft observations are included and averaged to a horizontal resolution of $4° \times 5°$.

[b]Due to data sparsity, the 5 HIPPO campaigns are averaged for calculation of vertical profiles.

[c]HIPPO vertical profiles are separated into North Pacific (35°N-60°N, 180°W-130°W), Central Pacific (35°S-35°N, 150°E-120°W), and South Pacific (70°S-35°S, 150°E-100°W).

[d]ATom vertical profiles are separated into North Pacific (35°N-60°N, 180°W-130°W), Central Pacific (35°S-35°N, 180°W-120°W), and South Pacific (70°S-35°S, 160°E-70°W).

[e]ATom vertical profiles are separated into North Atlantic (35°N-60°N, 60°W-0°E) and Central Atlantic (35°S-35°N, 40°W-0°E).

[f]INTEX-B vertical profiles are calculated separately for the two aircraft: DC-8 (19°N-60°N, 175°E-120°W) and C-130 (35°N-55°N, 140°W-105°W).

[g]PEM-Tropics A vertical profiles are separated into Central Pacific (35°S-35°N, 150°E-100°W), and South Pacific (70°S-35°S, 165°E-100°W).

jor differences in the global simulation between the two resolutions. We use a vertical resolution of 47 levels from the surface to 0.01 hPa, with some native GEOS-FP levels lumped in the stratosphere.

We include four new $RONO_2$ species: methyl nitrate (CH_3ONO_2, referred to here as $MeNO_3$), ethyl nitrate ($C_2H_5ONO_2$, referred to here as $EtNO_3$), and n-propyl and isopropyl nitrates ($C_3H_7ONO_2$, referred to here as n-$PrNO_3$ and i-$PrNO_3$ or their sum $PrNO_3$) respectively. Treatment of these species is detailed in the following sub-sections.

2.1 Ocean $RONO_2$ Flux

Measurements of enhanced $RONO_2$ in the marine boundary layer suggest an ocean source in both the tropics [*Atlas et al.*, 1993; *Blake et al.*, 2003] and the high southern latitudes [*Blake et al.*, 1999; *Jones et al.*, 1999; *Fischer et al.*, 2002]. In the tropics, this source has been confirmed by coincident atmospheric and seawater measurements showing high $MeNO_3$ and $EtNO_3$ supersaturation anomalies in both the Atlantic [*Chuck*, 2002] and Pacific [*Dahl et al.*, 2005]. The origin of the atmospheric enhancement over the Southern Ocean is less clear, with a small shipborne dataset showing tightly coupled atmosphere and ocean concentrations but only occasional supersaturation [*Hughes et al.*, 2008].

The mechanism for oceanic $RONO_2$ formation remains uncertain. Experimental evidence points to aqueous phase reaction between photochemically-produced NO and RO_2 radicals as a likely $RONO_2$ source in surface waters [*Moore and Blough*, 2002; *Dahl et al.*, 2003]. Seawater $RONO_2$ production is generally limited by available nitrite [*Dahl and Saltzman*, 2008], which photolyses to produce NO radicals [*Zafiriou and McFarland*, 1981; *Olasehinde et al.*, 2010; *Anifowose and Sakugawa*, 2017]. In dark environments (e.g., at depth) heterotrophic bacteria can provide an additional $RONO_2$ source, potentially via production of NO radicals [*Kim et al.*, 2015a].

Few seawater observations are available to constrain the global distribution of $RONO_2$ in the ocean. Representing the ocean-atmosphere flux of $RONO_2$ in global atmospheric models is therefore a challenge. *Neu et al.* [2008] calculated the flux using a single average Pacific Ocean value for the concentration gradient across the ocean-atmosphere interface, which they then scaled to fit aircraft observations over the tropics (10°S-10°N) and Southern Ocean (south of 45°S). Neither seasonal variability nor spatial variability within each basin were accounted for, and emissions outside these regions were as-

sumed to be negligible. More recent simulations [*Williams et al.*, 2014; *Khan et al.*, 2015] have simply applied variants of the *Neu et al.* [2008] fluxes as an oceanic emission.

Here, we instead apply a mechanistic treatment of bi-directional $RONO_2$ air-sea exchange that couples the flux to sea surface $MeNO_3$ and $EtNO_3$ concentrations and includes seasonal and spatial variability driven by dynamic changes in wind speed, sea surface temperature, and nitrite availability. We find from a model sensitivity simulation that the ocean $PrNO_3$ flux is too small to significantly impact the atmospheric simulation and do not include it here. We define ocean concentrations of $MeNO_3$ and $EtNO_3$ as described below. Air-sea exchange then follows *Johnson* [2010] with updated Henry's Law coefficients from the *Sander* [2015] compilation. The air-sea exchange parameterisation depends on both sea surface temperature and wind speed, which vary with the spatial ($2^\circ \times 2.5^\circ$) and temporal (hourly) resolution of the input GEOS-FP meteorology. While we do not explore interannual variability in $RONO_2$ air-sea exchange in this work, our parameterisation would enable future studies of this nature (for example, the impact of the El Niño-Southern Oscillation on air-sea exchange through changes in wind speed and temperature).

Seawater $RONO_2$ measurements are too rare to define a global distribution. Instead, we link seawater concentrations to nitrite distributions based on the experimental evidence that NO derived from nitrite is generally the limiting factor for ocean $RONO_2$ production [*Dahl and Saltzman*, 2008; *Dahl et al.*, 2012]. To our knowledge, no global spatially-resolved ocean nitrite dataset exists. We instead identify broad spatial regimes with non-zero sea surface nitrite using observations from three datasets: the Repeat Hydrography Cruises coordinated by NOAA through the U.S Global Ocean Carbon and Repeat Hydrography Program (available from `https://cchdo.ucsd.edu/search?q=USHYDRO`), the GEOSECS v2 Hydrographic and Tracer Data (available via Ocean Data View, `https://odv.awi.de/data/ocean/geosecs/`), and a dataset compiled by J. L. Reid and A. W. Mantyla (available via Ocean Data View, `https://odv.awi.de/data/ocean/reid-mantyla/`). The data are sparse, but comparing the three datasets shows that non-zero nitrite is generally found in the Southern Ocean south of 40°S, north of 40°N in the Pacific and north of 50°N in the Atlantic, and in the tropics from 15°S-10°N. We consider these as regions where $RONO_2$ production is possible.

In the tropics, *Dahl et al.* [2007] showed that $RONO_2$-enriched waters also have elevated chlorophyll, a relationship that is attributed to co-variation between chlorophyll and nitrite availability (rather than direct $RONO_2$ production by phytoplankton). Satellite-derived chlorophyll provides seasonally and spatially resolved information that is not available via the in situ nitrite datasets. We further refine our tropical $RONO_2$ source using MODIS monthly mean chlorophyll *a* concentrations from the year 2003, requiring chlorophyll >0.1 mg m^{-3}. We apply this requirement only in the tropics, where the empirical relationship has been observed. Our parameterisation does not take into account interannual variability in either nitrite or chlorophyll, which could be significant in the tropics (e.g., during different phases of the El Niño-Southern Oscillation). Nonetheless, our parameterisation captures the large-scale features of the atmospheric observations collected over multiple years (section 3). We also find that including this chlorophyll-derived nitrite proxy improves simulation of $RONO_2$ in the tropical marine boundary layer relative to a version that allowed $RONO_2$ production in all tropical waters.

We set fixed seawater $RONO_2$ concentrations in model grid squares where the nitrite and chlorophyll requirements are met. Elsewhere, the ocean is a sink for $MeNO_3$ and $EtNO_3$. Drivers of site-to-site variability are poorly understood, and so we apply a single ocean $MeNO_3$ concentration in each region, based where possible on seawater measurements. As $MeNO_3$ has not been measured in the northern high latitudes, we originally applied the same concentration value in the northern and southern high latitudes, but found this led to large biases relative to the aircraft data in the North Pacific. Our final seawater $MeNO_3$ concentrations are 400 pM in the tropics (upper limit from *Dahl et al.* [2007]), 200 pM in the southern high latitudes (upper limit from *Hughes et al.* [2008]), and 120 pM in the northern high latitudes (chosen to fit the atmospheric observations). We also apply a small $MeNO_3$ concentration of 25 pM in low-chlorophyll tropical waters based on the Warm Pool measurements from *Dahl et al.* [2007]. We set fixed $EtNO_3$ concentrations using an assumed 6:1 ratio of ocean $MeNO_3$:$EtNO_3$ [*Dahl et al.*, 2007].

Figure 1 shows the simulated annual mean net ocean-atmosphere $MeNO_3$ flux; the $EtNO_3$ flux shows the same pattern but with lower values. As seen in the figure, on an annual timescale the net flux is positive in the tropics and high latitudes, consistent with observations of an oceanic source to the atmosphere. Elsewhere (i.e., in regions assumed incompatible with seawater $RONO_2$ production), the ocean is always a small net sink. Spatial variability across the tropics comes from the chlorophyll-based constraint. In all

regions, the flux varies seasonally with changes in wind speed and sea surface temperature (right panels of Figure 1).

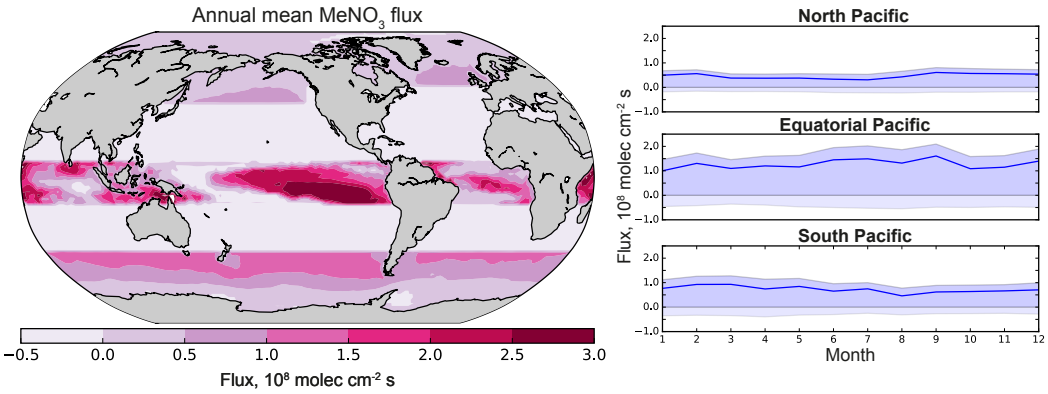

Figure 1. Net ocean-to-atmosphere flux of methyl nitrate ($MeNO_3$) in GEOS-Chem. Left: annual mean flux for all ocean grid squares. Right: Seasonal cycle of the net (solid line), upward (dark shading), and downward (light shading) flux in the North Pacific (130-180°W, 40-60°N), Equatorial Pacific (130-180°W, 15°S-10°N), and South Pacific (130-180°W, 40-70°S).

2.2 Chemistry

Chemical production of $RONO_2$ occurs via reaction of a VOC-derived peroxy radical ($RO_2^{\cdot}$) with NO (reactions 1-4). We do not consider $RONO_2$ from $RO^{\cdot}+NO_2$ reaction in fire plumes [*Simpson et al.*, 2002] as this source contributes less than 2% of the global $RONO_2$ budget [*Williams et al.*, 2014; *Khan et al.*, 2015]. We assume the dominant sources of the methyl, ethyl, and propyl $RO_2^{\cdot}$ radicals are reactions 1-2 (i.e., oxidation of methane, ethane, and propane, respectively). These $RO_2^{\cdot}$ radicals can also be produced during degradation of larger VOCs (including alkanes, aldehydes, and ketones) that are lumped in the GEOS-Chem mechanism. Standard treatment of the $RO_2^{\cdot}$ produced from degradation of lumped species in GEOS-Chem has historically been inconsistent. For species derived from lumped alkanes, the mechanism assumes an $RO_2^{\cdot}$ distribution of 50% (by carbon) ethyl peroxy, 40% isopropyl peroxy, and 10% n-propyl peroxy. Other lumped species produce only ethyl peroxy, based on the assumption that higher aldehydes react like propanal and higher ketones like methyl ethyl ketone [*Horowitz et al.*, 1998].

We find that this configuration overestimates $EtNO_3$ by a factor of 3-4 in both near-source and remote regions and underestimates $PrNO_3$ by a factor of 2 in source regions. Tracing the exact composition of the $RO_2^{\cdot}$ radical pool would require specifying the fraction of lumped species that come from each component VOC—information that we do not have. Instead, we find that we can reproduce observed $EtNO_3$ to first order across a range of environments by removing the ethyl peroxy source from lumped species. To avoid adverse effects on other model species, we replace model ethyl peroxy from higher VOC degradation with a generic $RO_2^{\cdot}$ radical that behaves like ethyl peroxy but does not form $EtNO_3$. For $PrNO_3$, we find that applying the assumptions already used in the model for alkane degradation (i.e., 40% isopropyl peroxy, 10% n-propyl peroxy, and 50% generic $RO_2^{\cdot}$) to aldehyde and ketone degradation yields a greatly improved simulation.

The $RONO_2$ yield from reaction 4 (i.e., the branching ratio between R4 and R3) is referred to as α and is a source of ongoing uncertainty in the $RONO_2$ budget, despite decades of experimental and computational study [*Dibble*, 2008]. For higher ($\geq C_2$) alkanes, $RONO_2$ production increases significantly with temperature [*Lee et al.*, 2014; *Nault et al.*, 2016]. Here we use empirically-derived $RONO_2$ yields that depend on temperature, pressure, and carbon number [*Carter and Atkinson*, 1989]. For methyl nitrate, *Butkovskaya et al.* [2012] measured the branching ratios at pressures representative of the upper troposphere and extrapolated these to the rest of the troposphere, resulting in a tropospheric-mean branching ratio of $\alpha = 1.0 \pm 0.7 \cdot 10^{-2}$. This value is roughly two orders of magnitude larger than previously derived by *Flocke et al.* [1998], who extrapolated results from a box model constrained by airborne measurements to derive a tropospheric branching ratio of $\alpha = 1.5 - 3.0 \cdot 10^{-4}$. *Williams et al.* [2014] tested both the *Flocke et al.* [1998] and *Butkovskaya et al.* [2012] yields and found the latter overestimated methyl nitrate observations by an order of magnitude. We similarly found that the *Butkovskaya et al.* [2012] yield led to a significant overestimate of $MeNO_3$ in GEOS-Chem. For this reason, we use a yield of $\alpha = 3.0 \cdot 10^{-4}$, the upper limit from *Flocke et al.* [1998].

Alkyl nitrates are predominantly removed by photolysis, followed by OH oxidation [*Clemitshaw et al.*, 1997; *Talukdar et al.*, 1997]. We use the Master Chemical Mechanism (MCM) version 3.3.1 to determine the products (mapped to GEOS-Chem species), with rate constants for OH oxidation from the JPL Data Evaluation v15-10 and photolysis cross sections from the MPI-Mainz UV/VIS Spectral Atlas (`http://satellite.mpic.`

de/spectral_atlas/cross_sections/), with NO_2 quantum yields of unity for all nitrates [*Higgins et al.*, 2014]. The full mechanism is given in the Supplement (Table S1).

Deposition is expected to be a minor sink for short-chain $RONO_2$ because of their very low solubility [*Perring et al.*, 2013]. However, observations suggest dry deposition can be an important sink for $MeNO_3$ in some environments [*Russo et al.*, 2010]. We include here a small dry deposition sink for all $RONO_2$, using the standard resistance-in-series scheme of *Wesely* [1989] with an assumed reactivity factor equivalent to that of NO_2 ($f_0 = 0.1$). Deposition to the ocean is included in our bi-directional ocean flux parameterisation, described in section 2.1.

2.3 Emissions

$RONO_2$ formation via reactions 1-4 requires both NO_x and precursor VOCs. For NO_x emissions, we use the configuration described in detail by *Travis et al.* [2016]. Briefly, fossil fuel NO_x comes from the EDGAR global inventory [*Olivier and Berdowski*, 2001], overwritten regionally with EMEP for Europe [*Vestreng and Klein*, 2002], *Zhang et al.* [2009] for Asia (increased by 25% based on satellite NO_2), NPRI for Canada (http://www.ec.gc.ca/inrp-npri/), BRAVO for Mexico [*Kuhns et al.*, 2005], and NEI2011 for the US (with modifications described by *Travis et al.* [2016]). Additional NO_x emissions come from the Quick Fire Emissions Database (QFED) [*Darmenov and Da Silva*, 2013] for biomass burning, *Hudman et al.* [2012] for soil and fertiliser, and *Murray et al.* [2012] for lightning.

Methane, ethane, and propane are the dominant VOC precursors to C_1–C_3 $RONO_2$ production (see section 2.2 for a discussion of other sources). We prescribe methane surface concentrations based on spatially kriged monthly mean flask observations collected by the NOAA Global Monitoring Division [*Murray*, 2016]. Above the surface layer, methane is treated as a standard model species subject to advection and chemistry.

We apply ethane emissions from the 2010 emission inventory from *Tzompa-Sosa et al.* [2017], obtained by combining scaled global estimates from a satellite methane inversion [*Turner et al.*, 2015] with the 2011 National Emissions Inventory (NEI) version 1 over the US. *Tzompa-Sosa et al.* [2017] showed that ethane distributions simulated using these emissions capture the seasonal and spatial distributions seen in surface and aircraft observations from around the world. $RONO_2$ sensitivity to recent changes in ethane

emissions driven by oil and gas extraction [*Helmig et al.*, 2014, 2016; *Dalsøren et al.*, 2018] is discussed in section 6.

Propane emissions are calculated following the same methodology as for ethane [*Tzompa-Sosa et al.*, 2017]. Globally, base emissions are scaled to the methane emissions of *Turner et al.* [2015] assuming a propane/methane mass ratio of 0.0663 kg kg^{-1} for biofuels [*Akagi et al.*, 2011] and 0.0932 kg kg^{-1} for oil and gas (based on emission ratios from *Katzenstein et al.* [2003] combined with enhancement ratios from *Kang et al.* [2014]). *Tzompa-Sosa et al.* [2017] previously showed that the *Turner et al.* [2015] emissions do not show a similar spatial distribution to known US oil and gas wells. To match the oil and gas distribution over the US, we use the NEI2011 inventory with the assumption that propane represents 3% of the lumped alkane species [*Yarwood et al.*, 2005; *Simon et al.*, 2010]. The resulting propane emissions are much too low relative to aircraft data collected near oil and gas sources (FRAPPE, 2014) and downwind (SEAC4RS, 2013). We find that to achieve good agreement with observations, we need to scale the NEI2011 inventory by a factor of 10. This large correction is consistent with recent work by *Dalsøren et al.* [2018], who found that simulated propane was roughly 2-5 times too low near US oil and gas sources even after increasing propane emissions by a factor of three. Our final simulations use the scaled *Turner et al.* [2015] emissions globally, overwritten over the US with NEI2011 emissions scaled by a factor of 10.

3 Global Distribution of C_1–C_3 Alkyl Nitrates

The simulated global mean burdens, lifetimes, and budget terms for C_1–C_3 $RONO_2$ are given in Table 2. On a global scale, $MeNO_3$ is 80% more abundant than $EtNO_3$ and $PrNO_3$ combined. Lifetimes range from 8 days for $PrNO_3$ to 14 days for $EtNO_3$ to 26 days for $MeNO_3$, within the large range estimated by previous studies [*Roberts and Fajer*, 1989; *Clemitshaw et al.*, 1997; *Talukdar et al.*, 1997; *Williams et al.*, 2014; *Khan et al.*, 2015]. The table highlights the importance of ocean exchange, which is responsible for two thirds of the $MeNO_3$ source and one third of the $EtNO_3$ source. Roughly 40% of the $RONO_2$ emitted by the ocean is subsequently lost to ocean uptake, close to an earlier estimate for $MeNO_3$ [*Williams et al.*, 2014, note ocean uptake was included with dry deposition in that work]. Nonetheless, chemical loss (including both photolysis and OH oxidation) is the main sink for all three species.

Table 2. Global mean burdens, lifetimes, and source/sink terms for C_1–C_3 alkyl nitrates in GEOS-Chem.

	Methyl Nitrate	Ethyl Nitrate	Propyl Nitrate
Burden (Gg N)	17	3.7	5.8
Lifetime (days)	26	14	8.3
Sources (Gg N a^{-1})			
Chemical production	81	66	254
Ocean emission	157	27	n/a
Sinks (Gg N a^{-1})			
Chemical loss [a]	165	76	221
Ocean uptake	58	11	n/a
Dry deposition	19	7	34

[a] Chemical loss includes both photodissociation and OH oxidation, which cannot be separated in the model diagnostics.

We evaluate the new $RONO_2$ simulation using a large dataset of airborne observations collected between 1996 and 2017. Names, dates, and locations of the campaigns are provided in Table 1. The campaigns were largely concentrated over the Pacific and North America, with seasonal coverage spanning all months except December. During the campaigns, whole air samples were collected in stainless steel canisters and analysed after the flights in off-site laboratories [for measurement details, see *Colman et al.*, 2001; *Atlas and UCAR/NCAR - Earth Observing Laboratory*, 2009]. Observations from pre-2008 aircraft campaigns have been scaled to account for changes to calibration, with scaling factors of 2.13 for $MeNO_3$, 1.81 for $EtNO_3$, and 1.24 for $PrNO_3$ [*Simpson et al.*, 2011].

Figures 2-4 show the annual mean distributions of methyl, ethyl and propyl nitrates as simulated by GEOS-Chem over three altitude bands, with airborne observations overplotted (gridded to $4°\times5°$ resolution). The three figures use the same color scale to facilitate comparison between species. The $MeNO_3$ distributions are also shown over a larger range of values in Figure S1 to highlight observed (gridded) values of up to 80 ppbv that are not apparent in Figure 2 due to the saturated color scale. The same observation-model comparisons are also presented as average vertical profiles for each campaign in the sup-

plement (Figures S2-S4). We compare all observations to a 2013 simulation but explore the sensitivity to changing emissions in section 6.

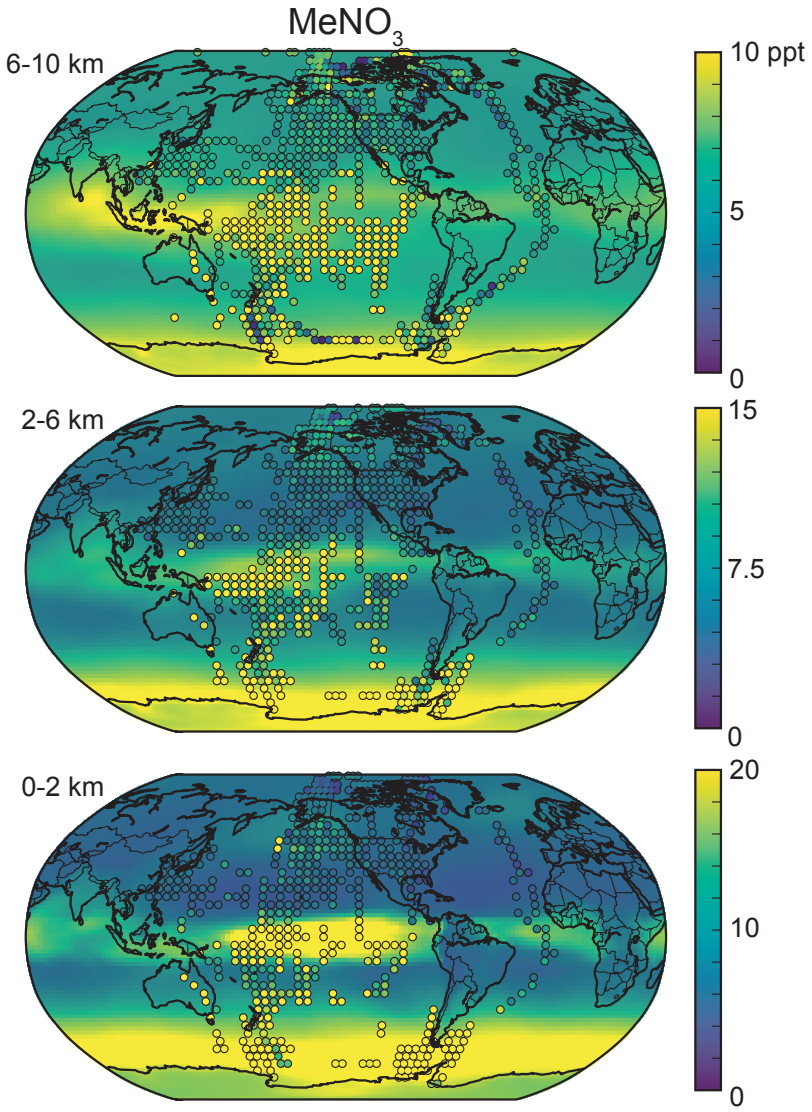

Figure 2. Annual mean distribution of methyl nitrate ($MeNO_3$) at different altitude ranges: 0-2 km (bottom), 2-6 km (middle), and 6-10 km (top). Solid background colors show model results from 2013 with aircraft observations from all years overplotted as filled circles. Observations have been averaged over all flight days and over a horizontal resolution of $4^\circ \times 5^\circ$ for visibility. Note the difference in color scale between different altitude ranges.

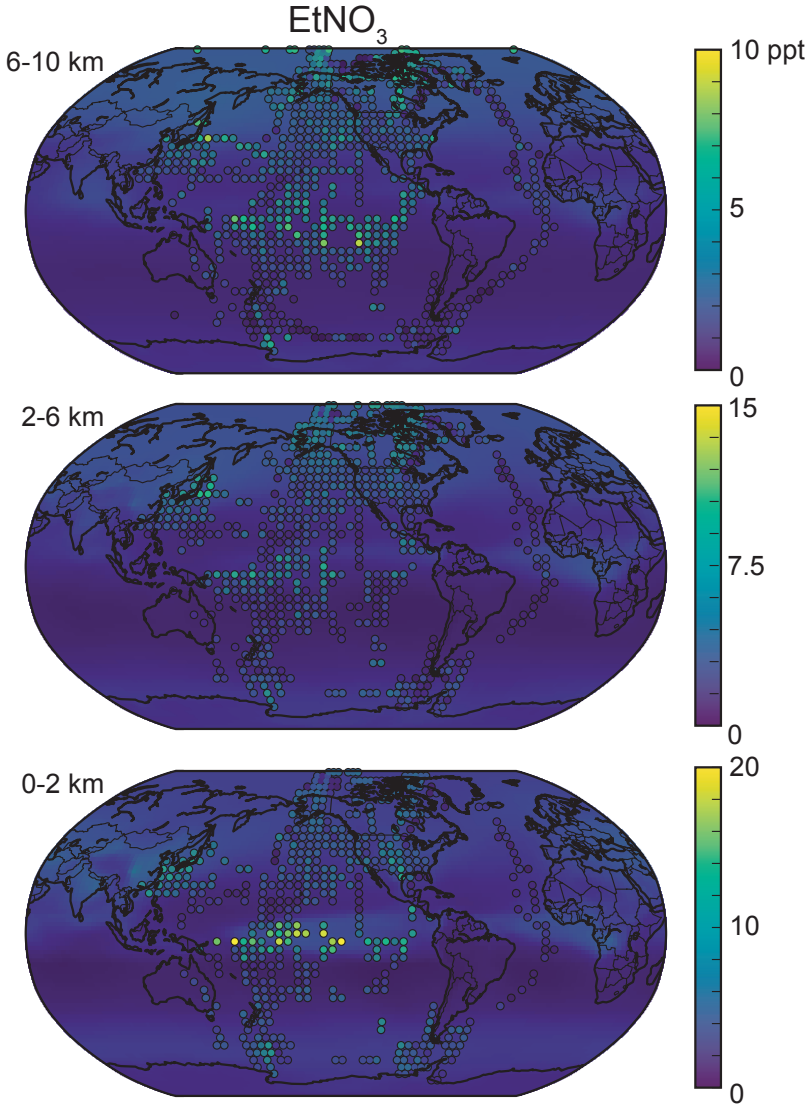

388 **Figure 3.** Same as Figure 2, but for ethyl nitrate ($EtNO_3$). The same color scales have been
389 used to facilitate comparison between species.

392 Both observations and model highlight differences in the global distributions of the
393 three species that are consistent with their sources and lifetimes. $MeNO_3$ is the dom-
394 inant form of $RONO_2$ except over the continents and near-shore outflow regions, where
395 $PrNO_3$ is larger. In these regions, elevated emissions of precursor VOCs, combined with
396 a higher yield for $PrNO_3$ formation than $MeNO_3$ or $EtNO_3$, drive enhanced $PrNO_3$ for-
397 mation. However, the $PrNO_3$ lifetime is short, and enhancements drop off rapidly with
398 altitude and with distance from source regions. Model underestimates of $PrNO_3$ in the

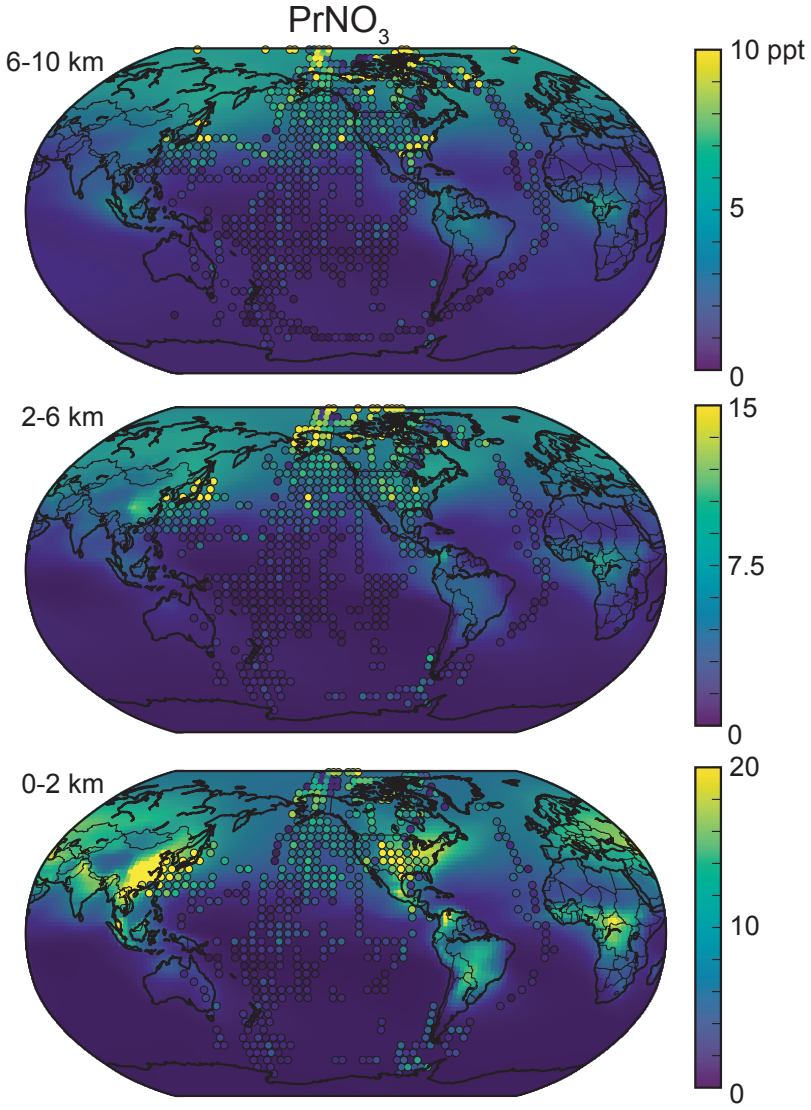

Figure 4. Same as Figure 2, but for propyl nitrate ($PrNO_3$). The same color scales have been used to facilitate comparison between species.

Arctic free troposphere may be driven by a low bias in propane emissions from Eurasian fossil fuel sources [*Dalsøren et al.*, 2018], which are readily transported to the Arctic in spring [*Shindell et al.*, 2008; *Fisher et al.*, 2010], when the Arctic campaigns took place (Table 1). Note that the $PrNO_3$ bias is not seen in the eastern North American Arctic (see TOPSE profile in Figure S4), consistent with the much slower transport from Eurasian sources to this part of the Arctic [*Fisher et al.*, 2010]. Over the North Pacific, the model somewhat underestimates boundary layer $PrNO_3$, suggesting the simulated lifetime may

be too short. However, low values in the Pacific free troposphere in both the model and the observations indicate $PrNO_3$ export is limited.

Elsewhere, $MeNO_3$ dominates the alkyl nitrate budget due to the large ocean source. The model generally captures the large-scale variability of $MeNO_3$, including the enhancements in the tropics and the southern high latitudes. The spatial structure is particularly well captured in the tropical marine boundary layer, where tying the ocean $MeNO_3$ concentrations to chlorophyll (as a proxy for nitrite availability) provides a better simulation of the $MeNO_3$ distribution than was achieved in a simulation using a latitude cut-off alone. In the free troposphere, the model underestimates the tropical observations by 30-50%. Evaluation against individual campaigns (Figure S2), however, suggests some discrepancy between the observations in this region. The model agrees well with the recent ATom campaigns (2016, 2017; mean bias = -1.3 ppt) but is biased low relative to the earlier PEM-Tropics campaigns (1996, 1999; mean bias = -6.6 ppt), which measured nearly twice as much $MeNO_3$ in the free troposphere. As shown in section 6, trends in VOC and NO_x emissions are unlikely to be responsible for this difference, and the discrepancy between the datasets remains unexplained.

$EtNO_3$ makes only a small contribution (<10 ppt) to total $RONO_2$ in all environments. As for $MeNO_3$, the model generally reproduces the spatial variability of boundary layer $EtNO_3$, with moderately elevated concentrations in the Southern Ocean, tropical Pacific, and parts of the North Pacific, but it is biased low throughout. In the tropical Pacific boundary layer, the low bias presumably reflects an underestimate in the prescribed ocean source (section 2.1). Elsewhere, the low bias is likely due to the treatment of the ethyl peroxy radical, which we assume here derives only from ethane oxidation but in reality has multiple chemical sources (see section 2.2). At only a few ppt, this bias has limited impact on the simulation of total $RONO_2$ and its impacts.

Figure 5 shows the seasonal distribution of total C_1–C_3 $RONO_2$ across a latitudinal transect through the Pacific Ocean (130-180°W). There appears to be little $RONO_2$ seasonality in the tropics, although large variability in the observations makes this difficult to verify. In the northern extratropics (north of 30°N), both observations and model show higher concentrations in winter than summer driven by the increased $RONO_2$ lifetime against photolysis and oxidation. The model underestimates polar tropospheric $RONO_2$ in boreal spring (MAM), mainly reflecting the $PrNO_3$ underestimate described above.

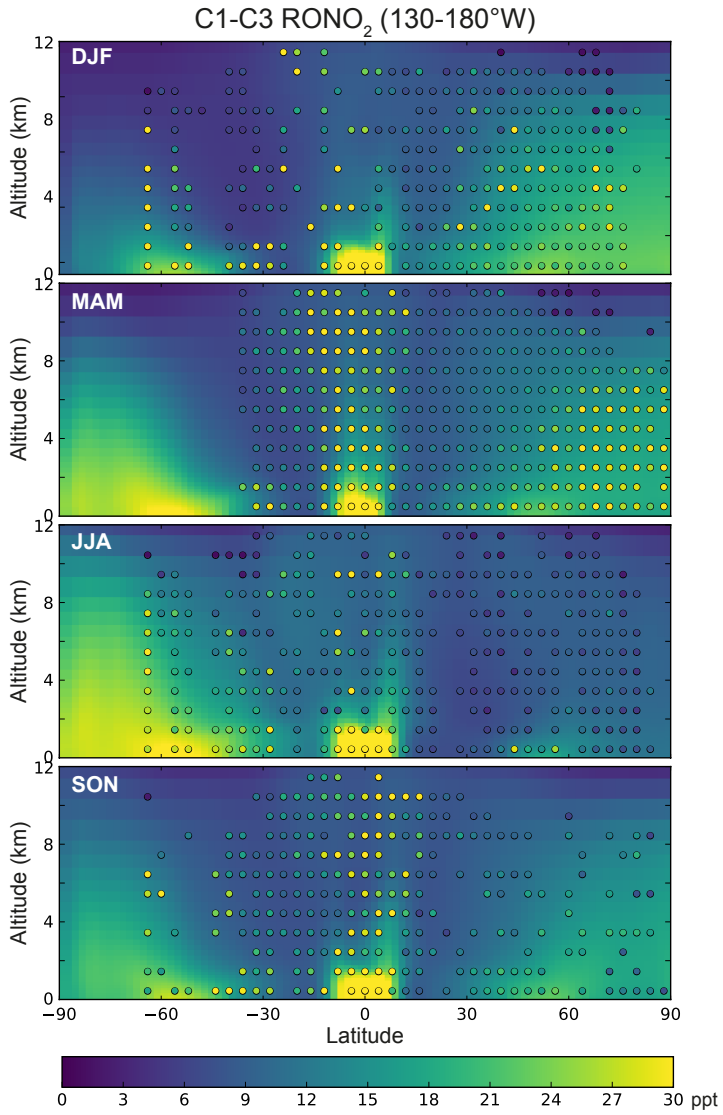

Figure 5. Zonal cross-sections of seasonal mean distribution of total C_1–C_3 $RONO_2$ over the Pacific (130-180°W). Solid background colors show model results from 2013, with aircraft observations from all years overplotted as filled circles. Observations have been averaged over all flight days and over a horizontal resolution of 4° × 5° and vertical resolution of 1 km.

The observations show the opposite $RONO_2$ seasonality in the southern high latitudes, with higher concentrations in austral summer (DJF) than winter (JJA) throughout the tropospheric column. The change is particularly apparent in the ATom data, which show a near doubling in $MeNO_3$ from ATom-1 in August 2016 to ATom-2 in February 2017 (Figure S2). The summer enhancement may be linked to a seasonal maximum in $RONO_2$ production in the Southern Ocean, particularly if ocean biota play a role [*Blake*

et al., 2003]. GEOS-Chem does not capture the observed seasonality in this region, showing significant $MeNO_3$ underestimates during the summer ATom-2 and ORCAS campaigns (Figure S2). The summer biases are largest near the surface, where the model is too low by 24% (ORCAS) to 48% (ATom-2). The model assumes constant seawater $RONO_2$ concentrations in the Southern Ocean, with values based on measurements taken in November/December [*Hughes et al.*, 2008]. Although no other seawater measurements are available to constrain this seasonality, a limited atmospheric dataset from the Antarctic continent suggests $MeNO_3$ increases throughout the summer [*Jones et al.*, 1999]. In late summer, seawater $RONO_2$ concentrations may therefore be higher than the early summer values used in the model, likely contributing to the atmospheric underestimate relative to the January-February ORCAS and ATom-2 data. Given the large contribution of $RONO_2$ to total reactive nitrogen in the southern high latitudes (see section 4), further observational constraints on seawater concentrations and fluxes in the Southern Ocean would provide significant value to atmospheric models.

4 Implications for Nitrogen and Ozone Budgets

We evaluate the impacts of C_1–C_3 $RONO_2$ by comparing the new simulation to a version of the model without these species but otherwise identical. Relative differences between the two simulations in both the boundary layer (0-2 km) and free troposphere (5-10 km) are shown in Figure 6 for NO_x, total reactive nitrogen ($NO_y \equiv NO_x + RONO_2 + PAN + HNO_3 +$ other nitrogen species), PAN and ozone. Absolute differences can be found in Figure S5 in the supplement.

The impacts of including $RONO_2$ in the simulation are most pronounced in the marine boundary layer of the tropical Pacific and the Southern Ocean, coincident with the large $MeNO_3$ source. In the absence of ocean-derived $RONO_2$, these regions have virtually no reactive nitrogen sources, and the added $RONO_2$ act to more than double boundary layer NO_y from a baseline of 20-25 ppt. In the free troposphere (right panels of Figures 6 and S5), NO_y increases nearly uniformly by 10-15 pptv, which equates to a nearly 20% enhancement over the tropical Pacific and Southern Ocean where NO_y is otherwise low. Increases in other NO_y components including NO_x and PAN appear large on a relative scale but are negligible (<1 ppt) in absolute terms (Figure S5).

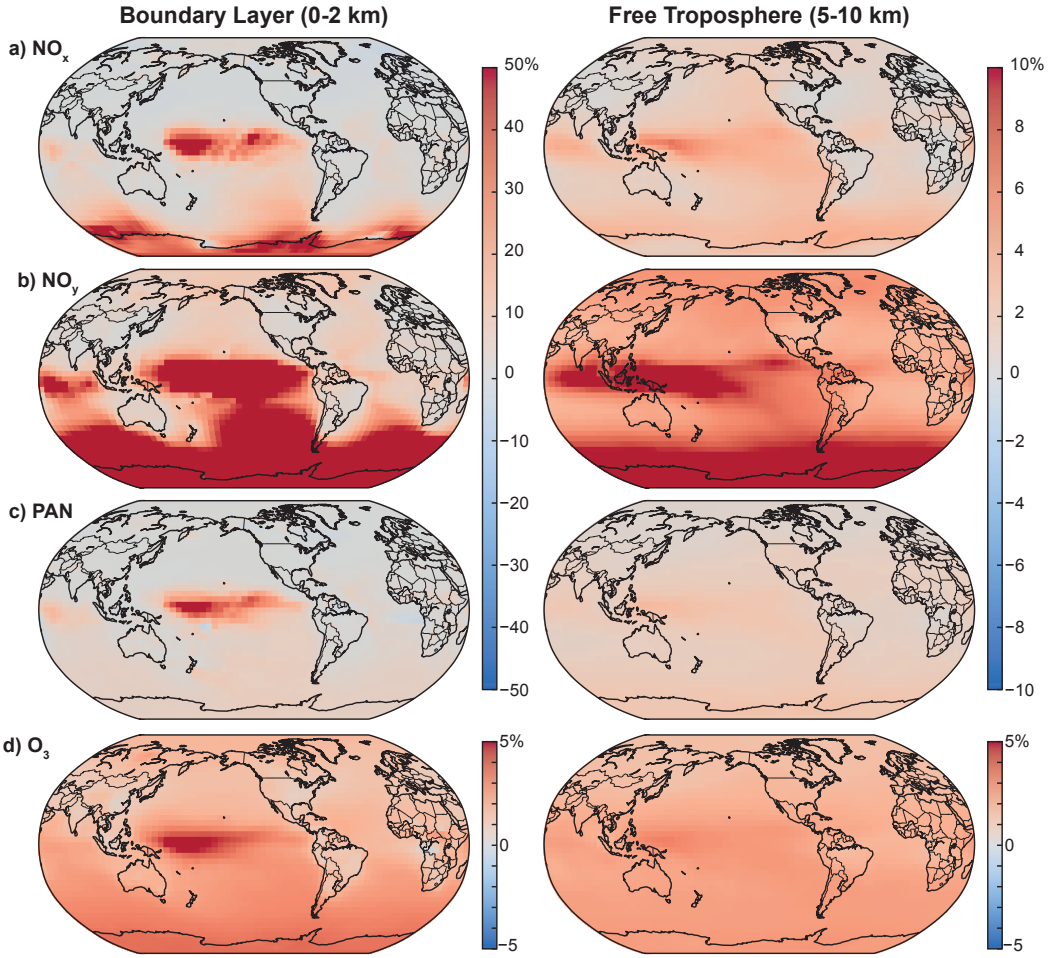

Figure 6. Relative change in annual mean (a) NO_x, (b) NO_y, (c) PAN, and (d) ozone caused by adding C_1–C_3 $RONO_2$ chemistry to GEOS-Chem. Changes are expressed as percent change from the standard simulation (no C_1–C_3 $RONO_2$) and shown separately for the boundary layer (0-2 km, left panels) and free troposphere (5-10 km, right panels). Absolute differences can be found in Figure S5.

Despite the large increase in reactive nitrogen over the Pacific, the average increase in ozone is less than 1 ppb, equivalent to up to 6.2% in the tropical marine boundary layer and closer to 3% in the free troposphere. The small impact on ozone found here is more consistent with the recent findings from *Williams et al.* [2014] than with the earlier work by *Neu et al.* [2008], who found an increase of up to 20%. As in *Williams et al.* [2014], we find that boundary layer ozone is well buffered and has limited sensitivity to the presence of alkyl nitrates.

Figure 7 shows the simulated NO_y partitioning along a latitudinal transect through the Pacific marine boundary layer (0-2 km, 180-130°W). In the northern hemisphere, the $RONO_2$ contribution is small relative to NO_x, HNO_3, and PAN. In the southern hemisphere, however, $RONO_2$ (mainly $MeNO_3$) are a significant source of nitrogen to the marine boundary layer, responsible for 20-60% of total NO_y. Consistent with the difference maps, the $RONO_2$ contribution is particularly significant in the tropics (15°S-10°N) and Southern Ocean (60-90°S), where it dominates the NO_y budget.

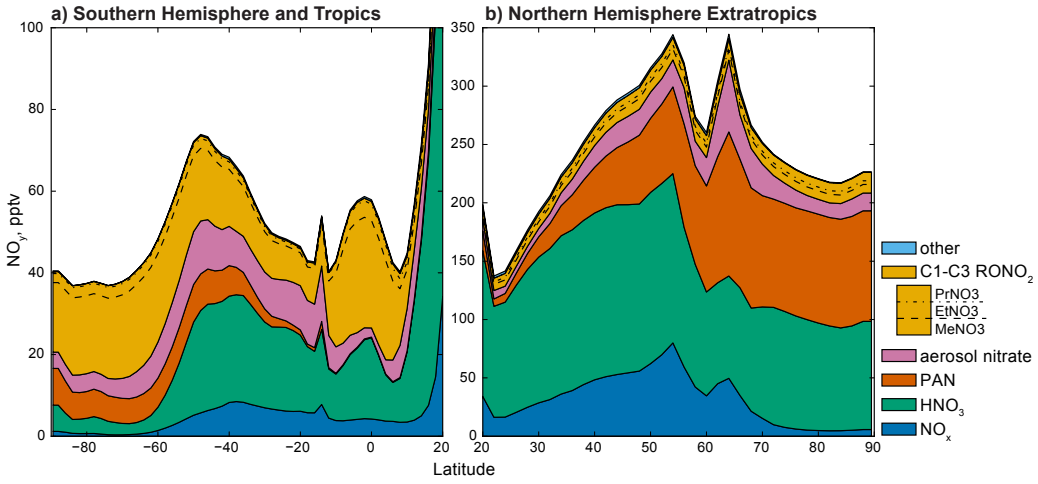

Figure 7. Simulated boundary layer (0-2 km) partitioning of NO_y as a function of latitude in the central Pacific Ocean (180-130°W).

Without including short-chain $RONO_2$, the model significantly underestimates reactive nitrogen over the Southern Ocean. Figure 8 compares vertical profiles of Southern Ocean NO_y observed during ATom to the original and improved simulations. The prior simulation (blue) underestimated NO_y in the South Pacific marine boundary layer by a factor of three in August (ATom-1) and by a factor of 15 in February (ATom-2). The figure suggests that $RONO_2$ can explain much of this discrepancy. When these species are included in GEOS-Chem (red), the NO_y bias disappears in August and is improved in February (from 15× to 3× too low). About half of the remaining difference in February can be explained by the summer $RONO_2$ underestimate described in section 3 (bottom panels of Figure 8).

Although the additional $RONO_2$ species greatly improve simulation of Southern Ocean NO_y, they do not explain a lingering model underestimate of NO_x in the region.

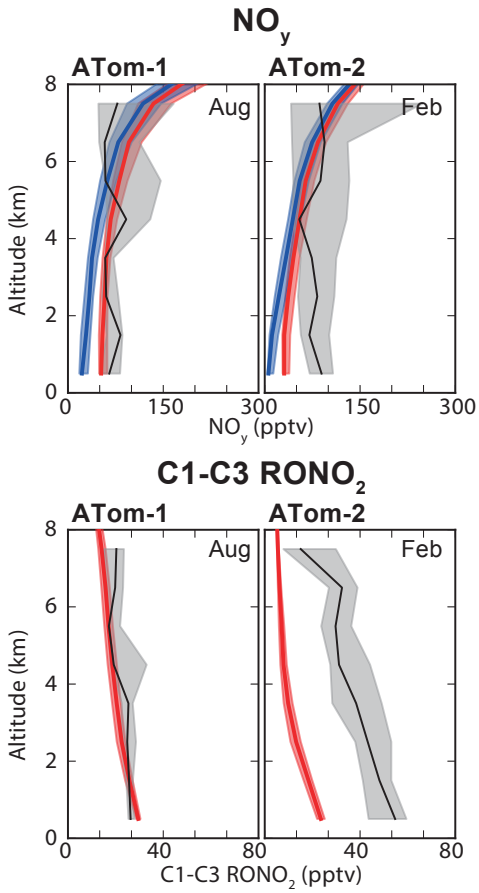

509 **Figure 8.** Observed (black) and simulated (red, blue) median vertical profiles of NO_y (top)
510 and C_1–C_3 $RONO_2$ (bottom) over the Southern Ocean (50-70°S, 175°E-70°W) during ATom-1
511 (Aug 2016) and ATom-2 (Feb 2017). For NO_y, the blue lines show the original simulation with
512 no C_1–C_3 $RONO_2$ and the red lines show the new simulation. Solid lines represent the median
513 value in 1-km altitude bins and shading represents the interquartile range.

516 Both the original and new simulations underestimate ATom NO_x observations by nearly
517 a factor of 20. There is negligible difference in NO_x between the two simulations (Fig-
518 ure S5), implying that $RONO_2$ degradation is not an important source of NO_x to the
519 Southern Ocean in the model. It is possible that the modelled $MeNO_3$ lifetime is too long,
520 leading to an underestimate of $RONO_2$ loss and associated NO_2 release, although the
521 lifetime (26 days, Table 2) is within the range of previous estimates [*Roberts and Fajer*,
522 1989; *Talukdar et al.*, 1997; *Butkovskaya et al.*, 2012; *Williams et al.*, 2014; *Khan et al.*,
523 2015]. If this is the case, our estimates of $RONO_2$ emission from the ocean are likely also

too low, as faster atmospheric loss would require a larger source to match observed atmospheric mixing ratios.

An alternative explanation for the missing Southern Ocean NO_x in the model is direct NO emission from the ocean, a source not included in GEOS-Chem. While one fate for NO radicals in seawater is reaction with dissolved organic matter to form $RONO_2$, an alternative is diffusion to the marine surface layer and exchange with the atmosphere (driven by the low solubility of NO in water). NO efflux has been observed in the equatorial Pacific [*Zafiriou and McFarland*, 1981; *Torres and Thompson*, 1993] as well as inland seas [*Olasehinde et al.*, 2010; *Anifowose and Sakugawa*, 2017], although it is typically much smaller than the deposition flux [*Liu et al.*, 1983]. Inclusion of a direct NO source from seawater could help reconcile observed and simulated atmospheric NO_x in the Southern Ocean. Measurements are needed to confirm whether this is a viable NO_x source in this region.

5 Contribution of Alkyl Nitrates to NO_x Export

The lifetimes of short-chain $RONO_2$ species are sufficiently long to allow their transport from sources to remote regions, and so they have the potential to serve as NO_x reservoirs. Chemical production of $RONO_2$ sequesters NO in high-emission source regions (reaction 4), while $RONO_2$ destruction via oxidation or photolysis releases NO_2 downwind. We use the new simulation to quantify the contribution of $RONO_2$ chemistry to NO_x export from source regions. For every model grid box, we calculate the net NO_x source/sink from $RONO_2$ chemistry ($\Delta NO_x|_{RONO_2}$) as the difference between NO consumed during $RONO_2$ formation ($P(NO_x)|_{RONO_2}$) and NO_2 released during $RONO_2$ destruction ($L(NO_x)|_{RONO_2}$):

$$\Delta NO_x|_{RONO_2} = P(NO_x)|_{RONO_2} - L(NO_x)|_{RONO_2} \quad (5)$$

We include here all $RONO_2$ species in the model mechanism to fully quantify the impact but expect the C_1–C_3 species to dominate export due to their longer lifetimes.

Figure 9a,b (top panels) shows the net NO_x source associated with $RONO_2$ chemistry. Orange pixels indicate net NO_x release (i.e., more NO_2 released than consumed in a given location) and purple pixels indicate net NO_x consumption. The figure shows

that $RONO_2$ are net NO_x sinks in continental regions, where emissions of precursors drive $RONO_2$ formation and associated NO consumption. In the tropics and southern hemisphere, $RONO_2$ are net NO_x sources over the oceans, presumably due to the direct ocean $RONO_2$ source coupled with a lack of precursors to enable in situ $RONO_2$ formation.

In contrast, $RONO_2$ drive net NO_x loss over the northern mid-latitude oceans. This result implies that $RONO_2$ do not effectively export NO_x from high-emission source regions to downwind ocean regions. The model indicates that $RONO_2$ destruction is enhanced in the northern mid-latitude continental outflow but is outweighed by enhanced in situ $RONO_2$ production (not shown). $RONO_2$ production requires available NO, implying the existence of an additional NO source in the continental outflow. The most likely NO sources to these heavily-travelled ocean regions are shipping emissions at the surface and aircraft emissions in the free troposphere. In the lower troposphere, PAN decomposition can also be a source of NO_x to the continental outflow, as discussed below.

We compare the net NO_x source from $RONO_2$ chemistry to the equivalent source from PAN in Figure 9c,d. PAN is stable at the cold temperatures of the mid-upper troposphere but unstable in the boundary layer. As a result, there is a strong vertical gradient in the net NO_x source from PAN, with NO_x release near the surface and NO_x consumption at higher altitude. The PAN-derived NO_x source is enhanced in the low-altitude continental outflow over the northern mid-latitudes, contributing to the NO_x available for $RONO_2$ production.

Outside the northern mid-latitude continental outflow, both $RONO_2$ and PAN are net sources of NO_x to the marine boundary layer. The source from PAN (Figure 9c) is generally larger than the source from $RONO_2$ (Figure 9a), except over the tropical Pacific. Here, PAN mixing ratios are at a minimum due to limited transport from source regions. At the same time, $RONO_2$ mixing ratios are enhanced by the direct ocean source. As a result, $RONO_2$ chemistry dominates the chemical NO_x source over the tropical marine boundary layer. In the free troposphere, the NO_x source from $RONO_2$ (Figure 9b) partly compensates for the NO_x sink to PAN formation (Figure 9d).

The bottom row in Figure 9 compares NO_x from $RONO_2$ to primary NO_x emissions, shown as the ratio between the two sources. As $RONO_2$ are a net sink for NO_x over the continents, the comparisons are only shown over the ocean. In most regions, the NO_x source from $RONO_2$ is much smaller than the source from primary emissions (ship-

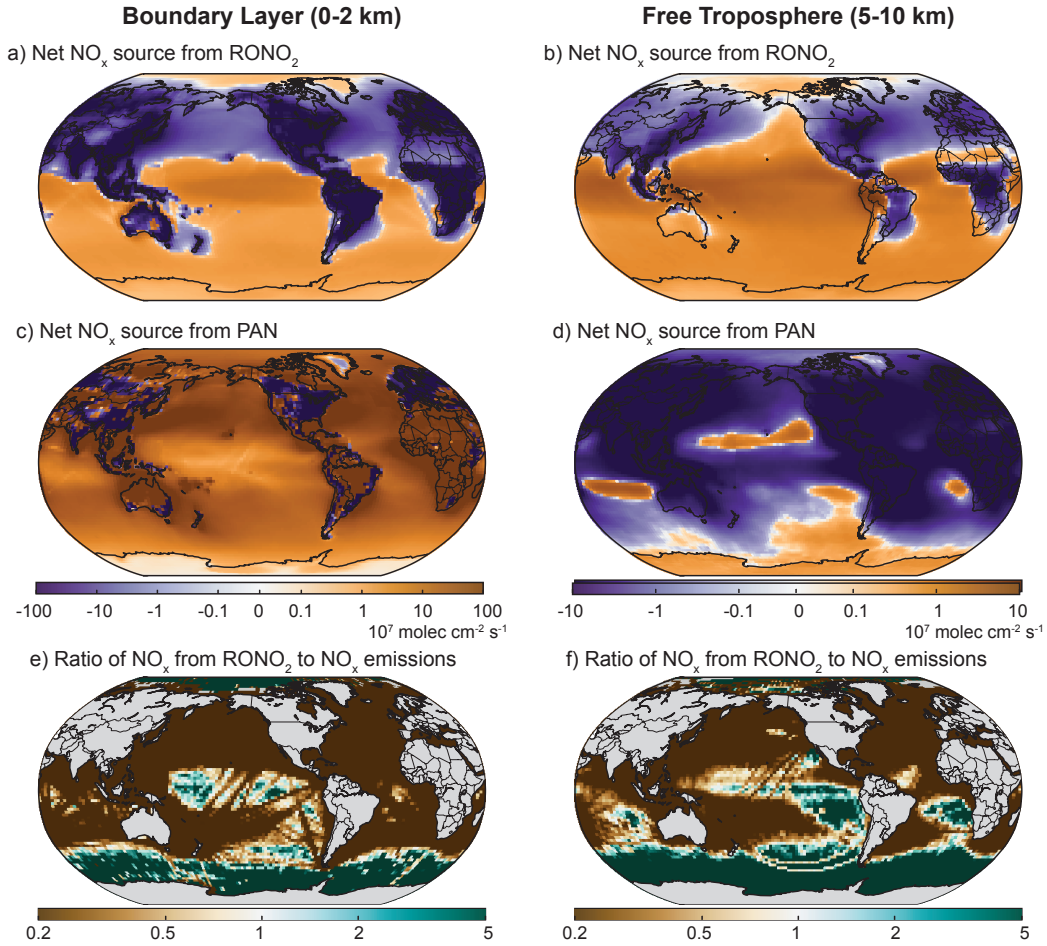

Figure 9. Impact of $RONO_2$ chemistry on NO_x export in the boundary layer (0-2 km, left) and free troposphere (5-10km, right). The net NO_x source from $RONO_2$ (a, b) is calculated as the difference between NO_2 release during $RONO_2$ decomposition and NO consumption during $RONO_2$ formation, and summed over model levels within the given altitude range. Orange areas indicate net NO_x release and purple indicate net NO_x loss. The net NO_x source from PAN (c, d) is calculated the same way. Note that the boundary layer and free troposphere values cannot be directly compared as they represent different altitudinal extents. The bottom figures (e, f) show the ratio between the NO_x source from $RONO_2$ and NO_x emissions. Areas with no net NO_x release from $RONO_2$ (all emissions) are shown in brown, and those with no NO_x emissions (all chemical) are shown in green.

ping, aircraft, and lightning). The two sources are roughly equivalent in parts of the tropics, where the ocean provides a direct $RONO_2$ source and primary emissions are low (outside major shipping and aircraft routes). Over the Southern Ocean where there are vir-

tually no primary emissions, $RONO_2$ degradation is the dominant NO_x source. Although the absolute amount of NO_x associated with the $RONO_2$ source is small, this result suggests a potentially significant perturbation to the chemistry of the Southern Ocean. Proper evaluation of the implications requires better understanding of the $RONO_2$ source in this region.

6 Sensitivity to Changing Emissions

In recent years, both NO_x and VOC emissions have changed dramatically. While global NO_x emissions have only grown slightly since 2000, there have been major changes in the distribution of source regions. Growing emissions from Asia, Africa, and Latin America have counteracted reductions in North America and Europe [*Hoesly et al.*, 2017]. Meanwhile, long-term declines in ethane and propane in the northern hemisphere [*Aydin et al.*, 2011; *Simpson et al.*, 2012; *Helmig et al.*, 2014] reversed in 2009 with significant growth linked to US oil and gas extraction [*Franco et al.*, 2016; *Helmig et al.*, 2016]. Around the same time, methane growth resumed after a stable period in the early 2000s [*Schaefer et al.*, 2016]. These changes to precursor emissions have implications for $RONO_2$. Here, we explore the sensitivity of the GEOS-Chem $RONO_2$ simulation to emission trends since 2000.

We performed three sensitivity simulations that are identical to the base simulation except using year 2000 emissions for: (1) NO_x only, (2) VOCs (methane, ethane, and propane) only, and (3) both NO_x and VOCs. The combined impact of changing both NO_x and VOC emissions was nearly identical to the impact of changing NO_x emissions alone, and so we do not discuss this simulation further. As described in section 2.3, NO_x and VOC emissions in our base simulation are derived by combining multiple inventories, with global emissions overwritten where available by regional inventories. Each inventory was originally derived using different methodologies and different base years (and so our "2013" emissions actually represent an amalgam of different years). As a result, it is not straightforward to simulate the impact of emission trends by replacing the "2013" base emissions with emissions from a global inventory for a different year.

Instead, we evaluate the relative change from 2000 to 2013 by applying regional scaling factors to the base emissions. NO_x scaling factors were calculated using the Community Emission Data System [*Hoesly et al.*, 2017], applied separately for the aggregated

regions defined therein (China, other Asia, Europe, Former Soviet Union, North America, Latin America, Africa, and global shipping). Ethane and propane scaling factors were derived from *Helmig et al.* [2016], who calculated 2009-2014 trends based on more than 30 sites. For ethane, we combined these with the pre-2009 trend from Jungfraujoch of roughly -1% yr^{-1}, which in the absence of further data we assume to be representative of the changing ethane background. For propane, we assume no trend before 2009 based on the reconstruction of *Helmig et al.* [2014]. Assumed regional 2000-2013 scaling factors for NO_x, ethane, and propane are provided in Table S2. Methane in our simulation is prescribed globally from surface in situ measurements (section 2.3), and so we use the observed 2000 values rather than applying a scaling factor.

Figure 10 shows that boundary layer $RONO_2$ and related chemistry are more sensitive to 2000–2013 changes in NO_x emissions (left panels) than changes in VOC emissions (right panels). Most of the change in total C_1–C_3 $RONO_2$ (Figure 10a,b) is found over the continental source regions, where it mirrors the changes in precursors (Table S2). Impacts are generally negligible over the oceans. The exception is the North Pacific, where the growth in East Asian NO_x emissions has led to enhanced export of $RONO_2$. Changes in the free troposphere are similar but more diffuse (Figure 11).

We also evaluate the implications for NO_x export via $RONO_2$ chemistry using $\Delta NO_x|_{RONO_2}$ (section 5), shown in Figure 10c,d for the boundary layer and Figure 11c,d for the free troposphere. In the marine boundary layer, changing NO_x emissions have largely driven decreases in the NO_x source from $RONO_2$. This suggests that a substantial fraction of the increased boundary layer $RONO_2$ in the continental outflow (Figure 10a) is formed in situ over the oceans, and that this $RONO_2$ production is in general NO_x-limited.

The situation is different in the free troposphere (Figure 11c,d). Here, $\Delta NO_x|_{RONO_2}$ increases across the North Pacific, including in the eastern North Pacific where $RONO_2$ are already a net NO_x source (orange regions in Figure 9). The figure also shows that for some regions in the central North Pacific, $RONO_2$ transition from being a net NO_x sink in 2000 to a net NO_x source by 2013. In other words, these results suggest $RONO_2$ have become increasingly important reservoirs for exporting NO_x from Asia to the North Pacific free troposphere.

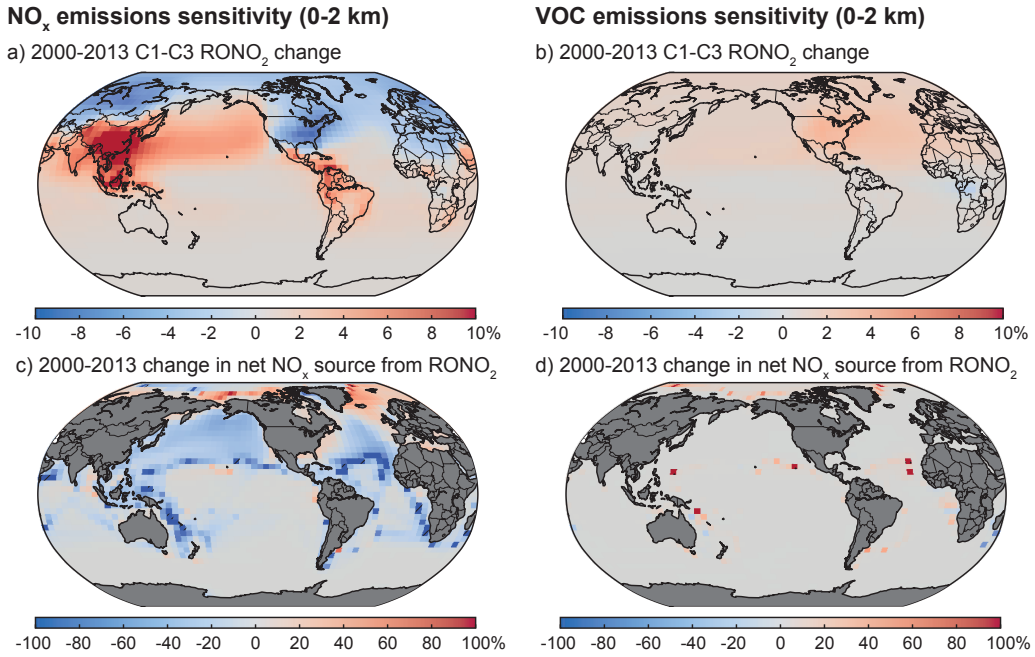

Figure 10. Sensitivity of boundary layer (0-2 km) C_1–C_3 $RONO_2$ (a, b) and related chemistry (c, d) to 2000-2013 changes in NO_x emissions (left) and VOC emissions (right). The net NO_x source from $RONO_2$ chemistry (c, d) is calculated as described in the text and in Figure 9; for clarity, only changes over the ocean are shown.

7 Conclusions

We have used a 20-year record of airborne observations combined with the GEOS-Chem chemical transport model to better understand the global sources, distribution, and impacts of three short-chain alkyl nitrates ($RONO_2$): methyl nitrate ($MeNO_3$), ethyl nitrate ($EtNO_3$), and propyl nitrate ($PrNO_3$). We modified GEOS-Chem to include the atmospheric chemical production and loss of these species, as well as their exchange with the ocean, and evaluated the simulation using the airborne observations. We then used the model to quantify the global budget and distribution of $MeNO_3$, $EtNO_3$, and $PrNO_3$, their impacts on the NO_x, reactive nitrogen, and ozone budgets (including through long-range export), and their sensitivity to recent changes in precursor emissions.

Our updated model provides for the first time a mechanistic treatment of bi-directional $RONO_2$ air-sea exchange. The new exchange parameterisation ties in situ seawater $RONO_2$ to the distribution of nitrite, a limiting factor for $RONO_2$ production [*Dahl and Saltzman*, 2008; *Dahl et al.*, 2012], with seawater concentrations based on the few existing

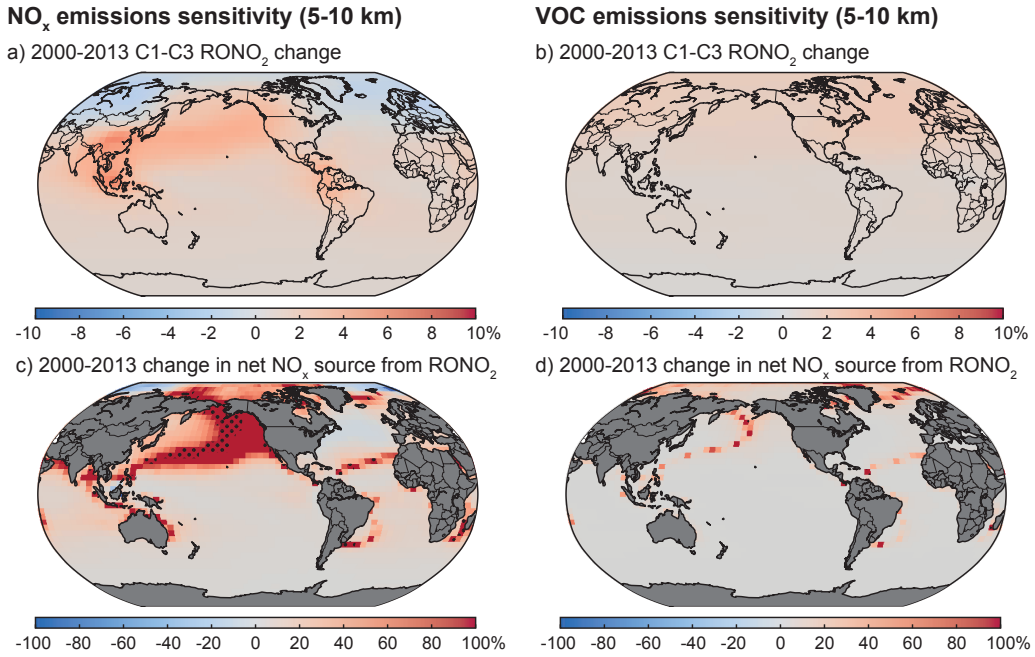

650 **Figure 11.** Same as Figure 10, but for the free troposphere (5-10 km). Stippling in (c, d)
651 highlights regions where $RONO_2$ changes from a net NO_x sink with 2000 emissions to a net NO_x
652 source with 2013 emissions.

680 waterside measurements [*Dahl et al.*, 2007; *Hughes et al.*, 2008]. The bi-directional ex-
681 change parameterisation improves on prior work by allowing the ocean to serve as both
682 a source and a sink for $RONO_2$, with both spatial and temporal variability driven by changes
683 in temperature, wind speed, and available nitrite. With the inclusion of bi-directional
684 $RONO_2$ ocean exchange combined with updates to the atmospheric chemistry and the
685 precursor emissions, the GEOS-Chem $RONO_2$ simulation is generally consistent with the
686 ensemble of airborne observations.

687 Both observations and model show that $MeNO_3$ accounts for the majority of global
688 C_1–C_3 $RONO_2$ (64%). $MeNO_3$ is the dominant form of $RONO_2$ everywhere except the
689 continental boundary layer, where $PrNO_3$ is more abundant due to a higher yield of for-
690 mation combined with elevated precursors. However, the short $PrNO_3$ lifetime limits its
691 contribution on the global scale (22%). $EtNO_3$ makes the smallest contribution globally
692 (14%), with concentrations that are substantially lower than $MeNO_3$ in marine environ-
693 ments and lower than $PrNO_3$ in continental environments. The large ensemble of air-
694 craft campaigns conducted at different times of year over the Pacific provides a unique

opportunity to evaluate $RONO_2$ seasonal variability. We find that the model captures the observed seasonality over the North Pacific, driven by the $RONO_2$ lifetime, and the lack of seasonality over the tropics. Over the South Pacific, GEOS-Chem underestimates the observed austral summer peak in $MeNO_3$ by roughly 50%. Better understanding of Southern Ocean seawater $RONO_2$ sources and ensuing fluxes is needed to improve $RONO_2$ simulations in this region.

We find in the model that $MeNO_3$ makes a large contribution to reactive nitrogen (NO_y) in the southern hemisphere marine boundary layer, particularly across the Southern Ocean where other NO_y sources are minimal. Here, $MeNO_3$ accounts for up to half of total simulated NO_y and corrects a large model NO_y underestimate relative to the ATom-1 aircraft observations (although the model remains low relative to the austral summer ATom-2 data). More modest impacts are seen for ozone, which increases by 6% in the tropical marine boundary layer but closer to 3% elsewhere. Impacts on marine NO_x are also small, with increases that are less than 1 pptv in absolute terms. Despite the introduction of a large $RONO_2$ source in the Southern Ocean, simulated NO_x in this region remains too low by a factor of 20. This large bias points to a missing NO_x source, possibly linked to direct NO emission from seawater, and requires further investigation.

The model indicates that $RONO_2$ do not play an important role in exporting NO_x from continental source regions to the remote marine environment. In fact, over the northern mid-latitudes, the polluted continental outflow is sufficiently enriched in $RONO_2$ precursors that $RONO_2$ production (NO_x-consuming) outweighs $RONO_2$ degradation (NO_x-releasing). Elsewhere, ocean-derived $RONO_2$ largely serve as a small net NO_x source. This source is generally smaller than the source from PAN degradation or from direct emissions but does become important in parts of the tropical free troposphere outside major aircraft and shipping channels.

Over the past decade, emissions of $RONO_2$ precursors have changed across the globe in response to both air quality policy and growing energy needs. We find using model sensitivity studies that growth in precursor VOCs since 2000 has had little impact on C_1–C_3 $RONO_2$. In contrast, increasing East Asian NO_x emissions have driven modest growth in North Pacific $RONO_2$ and an associated increase in net NO_x release in the remote free troposphere. While further increases in East Asian NO_x emissions are unlikely, business-as-usual scenarios predict substantial NO_x emissions growth in southern

Africa, South America, and Southeast Asia [*Turnock et al.*, 2018]. Our results imply that such growth may lead to enhanced $RONO_2$ and associated NO_x release over downwind ocean regions in the southern hemisphere and tropics—regions that are already among the most sensitive to $RONO_2$ cycling.

Acronyms

ARCTAS Arctic Research of the Composition of the Troposphere from Aircraft and Satellites

ATom Atmospheric Tomography

BRAVO Big Bend Regional Aerosol and Visibility Observational

DC3 Deep Convective Clouds and Chemistry

EDGAR Emission Database for Global Atmospheric Research

EMEP European Monitoring and Evaluation Programme

FRAPPE Front Range Air Pollution and Photochemistry Experiment

GEOS Goddard Earth Observing System

GEOSECS Geochemical Ocean Sections Study

HIPPO HIAPER Pole-to-Pole Observations

INTEX Intercontinental Chemical Transport Experiment

ITCT Intercontinental Transport and Chemical Transformation

JPL Jet Propulsion Laboratory

MCM Master Chemical Mechanism

NEI National Emissions Inventory

NOAA National Oceanographic and Atmospheric Administration

NPRI National Pollutant Release Inventory

ORCAS O2/N2 Ratio and CO2 Airborne Southern Ocean Study

PAN Peroxy Acetyl Nitrate

PEM-Tropics Pacific Exploratory Mission-Tropics

QFED Quick Fire Emissions Database

SEAC4RS Studies of Emissions and Atmospheric Composition, Clouds and Climate Coupling by Regional Surveys

TEXAQS Texas Air Quality Study

TOPSE Tropospheric Ozone Production about the Spring Equinox

TRACE-P TRAnsport and Chemical Evolution over the Pacific

VOC Volatile Organic Compound

Acknowledgments

We gratefully acknowledge the many contributors to all aspects of the 19 aircraft campaigns included here. We also thank Elisabeth Dahl for helpful discussions about the ocean source of alkyl nitrates. This work was funded in part by ARC Discovery Project DP160101598 and was undertaken with the assistance of resources provided at the NCI National Facility systems at the Australian National University through the National Computational Merit Allocation Scheme supported by the Australian Government. E.L.A. acknowledges contributions from F. Flocke, S. Schauffler, R. Lueb, R. Hendershot, V. Stroud, V. Donets, X. Zhu, M. Navarro and L. Pope, and financial support in several grants from NASA and and the NSF Atmospheric Chemistry Program. Funding for Z.A.T.-S. was provided by Consejo Nacional de Ciencia y Tecnologa (CONACYT) under fellowship No. 216028 and NOAA under award number NA14OAR4310148. Funding for ATom NO_y measurements was provided by the NASA Earth Venture Suborbital - 3 program #NNH15AB12I.

Aircraft data used in this work are available from: the Toolsets for Airborne Data Web Application (`https://tad.larc.nasa.gov/login.php`) for ARCTAS, INTEX, and TEXAQS; the NASA Airborne Science Data for Atmospheric Composition archive (`https://www-air.larc.nasa.gov/index.html`) for DC3, FRAPPE, SEAC4RS, and TRACE-P; the Global Tropospheric Experiment archive (`https://www-gte.larc.nasa.gov/gte_miss.htm`) for PEM-Tropics; the NCAR/UCAR Earth Observing Laboratory archive (`https://www.eol.ucar.edu/all-field-projects-and-deployments`) for HIPPO, ORCAS, and TOPSE; the NOAA Earth Systems Research Laboratory Chemical Sciences Division for ITCT (`https://esrl.noaa.gov/csd/projects/itct/2k2/`); and the NASA Earth Science Project Office Data Archive (`https://espoarchive.nasa.gov/archive/browse`) for ATom.

The standard GEOS-Chem code is freely accessible to the public by following the guidelines at `http://geos-chem.org/`. Updates described here will be included in the standard code once this paper has been accepted. In the interim, the modified version 9-02 code used here is available from `https://github.com/jennyfisher/Code.v9-02`.

`C1-C3_RONO2` with associated run directory files available from `https://github.com/jennyfisher/C1-C3_RONO2_chemistry`.

References

Akagi, S. K., R. J. Yokelson, C. Wiedinmyer, M. J. Alvarado, J. S. Reid, T. Karl, J. D. Crounse, and P. O. Wennberg (2011), Emission factors for open and domestic biomass burning for use in atmospheric models, *Atmospheric Chemistry and Physics*, *11*(9), 4039–4072.

Anifowose, A. J., and H. Sakugawa (2017), Determination of Daytime Flux of Nitric Oxide Radical (NO•) at an Inland Sea-Atmospheric Boundary in Japan, *Journal of Aquatic Pollution and Toxicology*, *1*(2), 1–6.

Atkinson, R., S. M. Aschmann, W. P. L. Carter, A. M. Winer, and J. N. Pitts (1982), Alkyl nitrate formation from the nitrogen oxide (NOx)-air photooxidations of C2-C8 n-alkanes, *The Journal of Physical Chemistry*, *86*(23), 4563–4569.

Atlas, E., W. Pollock, J. Greenberg, L. Heidt, and A. M. Thompson (1993), Alkyl nitrates, nonmethane hydrocarbons, and halocarbon gases over the equatorial Pacific Ocean during SAGA 3, *Journal of Geophysical Research*, *98*(D9), 16,933–16,947.

Atlas, E. L., and UCAR/NCAR - Earth Observing Laboratory (2009), Advanced Whole Air Sampler (AWAS) for HIAPER.

Aydin, M., K. R. Verhulst, E. S. Saltzman, M. O. Battle, S. A. Montzka, D. R. Blake, Q. Tang, and M. J. Prather (2011), Recent decreases in fossil-fuel emissions of ethane and methane derived from firn air, *Nature*, *476*(7359), 198–201.

Blake, N. J., D. R. Blake, O. W. Wingenter, B. C. Sive, C. H. Kang, D. C. Thornton, A. R. Bandy, E. Atlas, F. Flocke, J. M. Harris, and F. S. Rowland (1999), Aircraft measurements of the latitudinal, vertical, and seasonal variations of NMHCs, methyl nitrate, methyl halides, and DMS during the First Aerosol Characterization Experiment (ACE 1), *Journal of Geophysical Research: Atmospheres*, *104*(D17), 21,803–21,817.

Blake, N. J., D. R. Blake, A. L. Swanson, E. Atlas, F. Flocke, and F. S. Rowland (2003), Latitudinal, vertical, and seasonal variations of C1-C4 alkyl nitrates in the troposphere over the Pacific Ocean during PEM-Tropics A and B: Oceanic and continental sources, *Journal of Geophysical Research: Atmospheres*, *108*(D2),

8242.

Butkovskaya, N., A. Kukui, and G. Le Bras (2009), Pressure and Temperature Dependence of Ethyl Nitrate Formation in the C2H5O2 + NO Reaction, *The Journal of Physical Chemistry A*, *114*(2), 956–964.

Butkovskaya, N., A. Kukui, and G. Le Bras (2012), Pressure and Temperature Dependence of Methyl Nitrate Formation in the CH3O2 + NO Reaction, *The Journal of Physical Chemistry A*, *116*(24), 5972–5980.

Carter, W. P. L., and R. Atkinson (1989), Alkyl nitrate formation from the atmospheric photoxidation of alkanes; a revised estimation method, *Journal of atmospheric chemistry*, *8*(2), 165–173.

Chuck, A. L. (2002), Direct Evidence for a Marine Source of C1 and C2 Alkyl Nitrates, *Science*, *297*(5584), 1151–1154.

Clemitshaw, K. C., J. Williams, O. V. Rattigan, D. E. Shallcross, K. S. Law, and R. Anthony Cox (1997), Gas-phase ultraviolet absorption cross-sections and atmospheric lifetimes of several C2C5 alkyl nitrates, *Journal of Photochemistry and Photobiology A: Chemistry*, *102*(2-3), 117–126.

Colman, J. J., A. L. Swanson, S. Meinardi, B. C. Sive, D. R. Blake, and F. S. Rowland (2001), Description of the Analysis of a Wide Range of Volatile Organic Compounds in Whole Air Samples Collected during PEM-Tropics A and B, *Analytical Chemistry*, *73*(15), 3723–3731.

Dahl, E. E., and E. S. Saltzman (2008), Alkyl nitrate photochemical production rates in North Pacific seawater, *Marine Chemistry*, *112*(3-4), 137–141.

Dahl, E. E., E. S. Saltzman, and W. J. de Bruyn (2003), The aqueous phase yield of alkyl nitrates from ROO + NO: Implications for photochemical production in seawater, *Geophysical Research Letters*, *30*(6), 919.

Dahl, E. E., S. A. Yvon Lewis, and E. S. Saltzman (2005), Saturation anomalies of alkyl nitrates in the tropical Pacific Ocean, *Geophysical Research Letters*, *32*(20), L20,817.

Dahl, E. E., S. A. Yvon Lewis, and E. S. Saltzman (2007), Alkyl nitrate (C1-C3) depth profiles in the tropical Pacific Ocean, *Journal of Geophysical Research: Atmospheres*, *112*(C1), C01,012.

Dahl, E. E., E. M. Heiss, and K. Murawski (2012), The effects of dissolved organic matter on alkyl nitrate production during GOMECC and laboratory studies,

Marine Chemistry, *142-144*, 11–17.

Dalsøren, S. B., G. Myhre, Ø. Hodnebrog, C. L. Myhre, A. Stohl, I. Pisso, S. Schwietzke, L. Höglund-Isaksson, D. Helmig, S. Reimann, S. Sauvage, N. Schmidbauer, K. A. Read, L. J. Carpenter, A. C. Lewis, S. Punjabi, and M. Wallasch (2018), Discrepancy between simulated and observed ethane and propane levels explained by underestimated fossil emissions, *Nature Geoscience*, *11*(3), 178–184.

Darmenov, A. S., and A. Da Silva (2013), The Quick Fire Emissions Dataset (QFED) - Documentation of versions 2.1, 2.2 and 2.4, *Tech. Rep. NASA/TM–2013–104606/*, Greenbelt, Maryland, USA.

Dibble, T. S. (2008), Failures and limitations of quantum chemistry for two key problems in the atmospheric chemistry of peroxy radicals, *Atmospheric Environment*, *42*(23), 5837–5848.

Farmer, D. K., A. E. Perring, P. J. Wooldridge, D. R. Blake, A. Baker, S. Meinardi, L. G. Huey, D. Tanner, O. Vargas, and R. C. Cohen (2011), Impact of organic nitrates on urban ozone production, *Atmospheric Chemistry and Physics*, *11*(9), 4085–4094.

Fischer, E. V., D. J. Jacob, R. M. Yantosca, M. P. Sulprizio, D. B. Millet, J. Mao, F. Paulot, H. B. Singh, A. Roiger, L. Ries, R. W. Talbot, K. Dzepina, and S. Pandey Deolal (2014), Atmospheric peroxyacetyl nitrate (PAN): a global budget and source attribution, *Atmospheric Chemistry and Physics*, *14*(5), 2679–2698.

Fischer, R., R. Weller, H.-W. Jacobi, and K. Ballschmiter (2002), Levels and pattern of volatile organic nitrates and halocarbons in the air at Neumayer Station (70?S), Antarctic, *Chemosphere*, *48*(9), 981–992.

Fisher, J. A., D. J. Jacob, M. T. Purdy, M. Kopacz, P. Le Sager, C. Carouge, C. D. Holmes, R. M. Yantosca, R. L. Batchelor, K. Strong, G. S. Diskin, H. E. Fuelberg, J. S. Holloway, E. J. Hyer, W. W. McMillan, J. Warner, D. G. Streets, Q. Zhang, Y. Wang, and S. Wu (2010), Source attribution and interannual variability of Arctic pollution in spring constrained by aircraft (ARCTAS ARCPAC) and satellite (AIRS) observations of carbon monoxide, *Atmospheric Chemistry and Physics*, *10*(3), 977–996.

Fisher, J. A., D. J. Jacob, K. R. Travis, P. S. Kim, E. A. Marais, C. Chan Miller, K. Yu, L. Zhu, R. M. Yantosca, M. P. Sulprizio, and others (2016), Organic nitrate chemistry and its implications for nitrogen budgets in an isoprene-and

monoterpene-rich atmosphere: constraints from aircraft (SEAC 4 RS) and ground-based (SOAS) observations in the Southeast US, *Atmospheric Chemistry and Physics*, *16*(9), 5969–5991.

Flocke, F., E. Atlas, S. Madronich, S. M. Schauffler, K. Aikin, J. J. Margitan, and T. P. Bui (1998), Observations of methyl nitrate in the lower stratosphere during STRAT: Implications for its gas phase production mechanisms, *Geophysical Research Letters*, *25*(11), 1891–1894.

Franco, B., E. Mahieu, L. K. Emmons, Z. A. Tzompa-Sosa, E. V. Fischer, K. Sudo, B. Bovy, S. Conway, D. Griffin, J. W. Hannigan, K. Strong, and K. A. Walker (2016), Evaluating ethane and methane emissions associated with the development of oil and natural gas extraction in North America, *Environmental Research Letters*, *11*(4), 044,010.

Geddes, J. A., and R. V. Martin (2017), Global deposition of total reactive nitrogen oxides from 1996 to 2014 constrained with satellite observations of NO2 columns, *Atmospheric Chemistry and Physics*, *17*(16), 10,071–10,091.

Helmig, D., V. Petrenko, P. Martinerie, E. Witrant, T. Röckmann, A. Zuiderweg, R. Holzinger, J. Hueber, C. Thompson, J. W. C. White, W. Sturges, A. Baker, T. Blunier, D. Etheridge, M. Rubino, and P. Tans (2014), Reconstruction of Northern Hemisphere 1950–2010 atmospheric non-methane hydrocarbons, *Atmospheric Chemistry and Physics*, *14*(3), 1463–1483.

Helmig, D., S. Rossabi, J. Hueber, P. Tans, S. A. Montzka, K. Masarie, K. Thoning, C. Plass-Duelmer, A. Claude, L. J. Carpenter, A. C. Lewis, S. Punjabi, S. Reimann, M. K. Vollmer, R. Steinbrecher, J. W. Hannigan, L. K. Emmons, E. Mahieu, B. Franco, D. Smale, and A. Pozzer (2016), Reversal of global atmospheric ethane and propane trends largely due to US oil and natural gas production, *Nature Geoscience*, *9*(7), 490–495.

Higgins, C. M., L. A. Evans, G. C. Lloyd-Jones, D. E. Shallcross, D. P. Tew, and A. J. Orr-Ewing (2014), Quantum Yields for Photochemical Production of NO 2from Organic Nitrates at Tropospherically Relevant Wavelengths, *The Journal of Physical Chemistry A*, *118*(15), 2756–2764.

Hoesly, R. M., S. J. Smith, L. Feng, Z. Klimont, G. Janssens-Maenhout, T. Pitkanen, J. J. Seibert, L. Vu, R. J. Andres, R. M. Bolt, T. C. Bond, L. Dawidowski, N. Kholod, J.-i. Kurokawa, M. Li, L. Liu, Z. Lu, M. C. P. Moura, P. R.

O amp apos Rourke, and Q. Zhang (2017), Historical (1750–2014) anthropogenic emissions of reactive gases and aerosols from the Community Emission Data System (CEDS), *Geoscientific Model Development Discussions*, pp. 1–41.

Horowitz, L. W., J. Liang, G. M. Gardner, and D. J. Jacob (1998), Export of reactive nitrogen from North America during summertime: Sensitivity to hydrocarbon chemistry, *Journal of Geophysical Research: Atmospheres*, *103*(D11), 13,451–13,476.

Hu, L., D. J. Jacob, X. Liu, Y. Zhang, L. Zhang, P. S. Kim, M. P. Sulprizio, and R. M. Yantosca (2017), Global budget of tropospheric ozone: Evaluating recent model advances with satellite (OMI), aircraft (IAGOS), and ozonesonde observations, *Atmospheric Environment*, *167*, 323–334.

Hudman, R. C., D. J. Jacob, O. R. Cooper, M. J. Evans, C. L. Heald, R. J. Park, F. Fehsenfeld, F. Flocke, J. Holloway, G. Hübler, K. Kita, M. Koike, Y. Kondo, A. Neuman, J. Nowak, S. Oltmans, D. Parrish, J. M. Roberts, and T. Ryerson (2004), Ozone production in transpacific Asian pollution plumes and implications for ozone air quality in California, *Journal of Geophysical Research: Atmospheres*, *109*(D23), 39.

Hudman, R. C., N. E. Moore, A. K. Mebust, R. V. Martin, A. R. Russell, L. C. Valin, and R. C. Cohen (2012), Steps towards a mechanistic model of global soil nitric oxide emissions: implementation and space based-constraints, *Atmospheric Chemistry and Physics*, *12*(16), 7779–7795.

Hughes, C., A. L. Chuck, S. M. Turner, and P. S. Liss (2008), Methyl and ethyl nitrate saturation anomalies in the Southern Ocean (36?65?S, 30?70?W), *Environmental Chemistry*, *5*(1), 11.

Johnson, M. T. (2010), A numerical scheme to calculate temperature and salinity dependent air-water transfer velocities for any gas, *Ocean Science*, *6*(4), 913–932.

Jones, A. E., R. Weller, A. Minikin, E. W. Wolff, W. T. Sturges, H. P. McIntyre, S. R. Leonard, O. Schrems, and S. Bauguitte (1999), Oxidized nitrogen chemistry and speciation in the Antarctic troposphere, *Journal of Geophysical Research: Atmospheres*, *104*(D17), 21,355–21,366.

Kang, M., C. M. Kanno, M. C. Reid, X. Zhang, D. L. Mauzerall, M. A. Celia, Y. Chen, and T. C. Onstott (2014), Direct measurements of methane emissions from abandoned oil and gas wells in Pennsylvania, *Proceedings of the National*

Academy of Sciences, *111*(51), 18,173–18,177.

Katzenstein, A. S., L. A. Doezema, I. J. Simpson, D. R. Blake, and F. S. Rowland (2003), Extensive regional atmospheric hydrocarbon pollution in the southwestern United States, *Proceedings of the National Academy of Sciences*, *100*(21), 11,975–11,979.

Khan, M. A. H., M. C. Cooke, S. R. Utembe, W. C. Morris, A. T. Archibald, R. G. Derwent, M. E. Jenkin, A. J. Orr-Ewing, C. M. Higgins, C. J. Percival, K. E. Leather, and D. E. Shallcross (2015), Global modeling of the C1-C3 alkyl nitrates using STOCHEM-CRI, *Atmospheric Environment*, *123*(Part A), 256–267.

Kim, M. J., J. M. Michaud, R. Williams, B. P. Sherwood, R. Pomeroy, F. Azam, M. Burkart, and T. H. Bertram (2015a), Bacteria-driven production of alkyl nitrates in seawater, *Geophysical Research Letters*, *42*(2), 597–604.

Kim, P. S., D. J. Jacob, J. A. Fisher, K. Travis, K. Yu, L. Zhu, R. M. Yantosca, M. P. Sulprizio, J. L. Jimenez, P. Campuzano-Jost, K. D. Froyd, J. Liao, J. W. Hair, M. A. Fenn, C. F. Butler, N. L. Wagner, T. D. Gordon, A. Welti, P. O. Wennberg, J. D. Crounse, J. M. St Clair, A. P. Teng, D. B. Millet, J. P. Schwarz, M. Z. Markovic, and A. E. Perring (2015b), Sources, seasonality, and trends of southeast US aerosol: an integrated analysis of surface, aircraft, and satellite observations with the GEOS-Chem chemical transport model, *Atmospheric Chemistry and Physics*, *15*(18), 10,411–10,433.

Kuhns, H., E. M. Knipping, and J. M. Vukovich (2005), Development of a United States–Mexico Emissions Inventory for the Big Bend Regional Aerosol and Visibility Observational (BRAVO) Study, *Journal of the Air & Waste Management Association*, *55*(5), 677–692.

Lee, L., P. J. Wooldridge, J. B. Gilman, C. Warneke, J. de Gouw, and R. C. Cohen (2014), Low temperatures enhance organic nitrate formation: evidence from observations in the 2012 Uintah Basin Winter Ozone Study, *Atmospheric Chemistry and Physics*, *14*(22), 12,441–12,454.

Liu, S. C., M. McFarland, D. Kley, O. Zafiriou, and B. Huebert (1983), Tropospheric NO x and O3 budgets in the equatorial Pacific, *Journal of Geophysical Research: Atmospheres (1984–2012)*, *88*(C2), 1360–1368.

Marais, E. A., D. J. Jacob, J. L. Jimenez, P. Campuzano-Jost, D. A. Day, W. Hu, J. Krechmer, L. Zhu, P. S. Kim, C. C. Miller, J. A. Fisher, K. Travis, K. Yu, T. F.

Hanisco, G. M. Wolfe, H. L. Arkinson, H. O. T. Pye, K. D. Froyd, J. Liao, and V. F. McNeill (2016), Aqueous-phase mechanism for secondary organic aerosol formation from isoprene: application to the southeast United States and co-benefit of SO2 emission controls, *Atmospheric Chemistry and Physics*, *16*(3), 1603–1618.

Moore, R. M., and N. V. Blough (2002), A marine source of methyl nitrate, *Geophysical Research Letters*, *29*(15), 27–1–27–4.

Murray, L. T. (2016), Lightning NO x and Impacts on Air Quality, *Current Pollution Reports*, *2*(2), 115–133.

Murray, L. T., D. J. Jacob, J. A. Logan, R. C. Hudman, and W. J. Koshak (2012), Optimized regional and interannual variability of lightning in a global chemical transport model constrained by LIS/OTD satellite data, *Journal of Geophysical Research: Atmospheres*, *117*(D20), 3851.

Nault, B. A., C. Garland, P. J. Wooldridge, W. H. Brune, P. Campuzano-Jost, J. D. Crounse, D. A. Day, J. Dibb, S. R. Hall, L. G. Huey, J. L. Jimenez, X. Liu, J. Mao, T. Mikoviny, J. Peischl, I. B. Pollack, X. Ren, T. B. Ryerson, E. Scheuer, K. Ullmann, P. O. Wennberg, A. Wisthaler, L. Zhang, and R. C. Cohen (2016), Observational Constraints on the Oxidation of NOx in the Upper Troposphere, *The Journal of Physical Chemistry A*, *120*(9), 1468–1478.

Neu, J. L., M. J. Lawler, M. J. Prather, and E. S. Saltzman (2008), Oceanic alkyl nitrates as a natural source of tropospheric ozone, *Geophysical Research Letters*, *35*(13), L13,814.

Olasehinde, E. F., K. Takeda, and H. Sakugawa (2010), Photochemical Production and Consumption Mechanisms of Nitric Oxide in Seawater, *Environmental Science & Technology*, *44*(22), 8403–8408.

Olivier, J. G. J., and J. J. M. Berdowski (2001), Global emissions sources and sinks, in *The Climate System*, edited by J. J. M. Berdowski, R. Guicherit, and B. J. Heij, pp. 33–78, Lisse, The Netherlands.

Paulot, F., D. J. Jacob, and D. K. Henze (2013), Sources and Processes Contributing to Nitrogen Deposition: An Adjoint Model Analysis Applied to Biodiversity Hotspots Worldwide, *Environmental Science & Technology*, *47*(7), 3226–3233.

Perring, A. E., T. H. Bertram, D. K. Farmer, P. J. Wooldridge, J. Dibb, N. J. Blake, D. R. Blake, H. B. Singh, H. Fuelberg, G. Diskin, G. Sachse, and R. C. Cohen (2010), The production and persistence of ΣRONO¡sub¿2¡/sub¿ in the

Mexico City plume, *Atmospheric Chemistry and Physics*, *10*(15), 7215–7229.

Perring, A. E., S. E. Pusede, and R. C. Cohen (2013), An Observational Perspective on the Atmospheric Impacts of Alkyl and Multifunctional Nitrates on Ozone and Secondary Organic Aerosol, *Chemical Reviews*, *113*(8), 5848–5870.

Ranschaert, D. L., N. J. Schneider, and M. J. Elrod (2000), Kinetics of the C2H5O2 + NOx Reactions: Temperature Dependence of the Overall Rate Constant and the C2H5ONO2 Branching Channel of C2H5O2 + NO, *The Journal of Physical Chemistry A*, *104*(24), 5758–5765.

Roberts, J. M., and R. W. Fajer (1989), UV absorption cross sections of organic nitrates of potential atmospheric importance and estimation of atmospheric lifetimes, *ACS Publications*, *23*, 945–951.

Roberts, J. M., D. D. Parrish, R. B. Norton, S. B. Bertman, J. S. Holloway, M. Trainer, F. C. Fehsenfeld, M. A. Carroll, G. M. Albercook, T. Wang, and G. Forbes (1996), Episodic removal of NOy species from the marine boundary layer over the North Atlantic, *Journal of Geophysical Research: Atmospheres*, *101*(D22), 28,947–28,960.

Russo, R. S., Y. Zhou, K. B. Haase, O. W. Wingenter, E. K. Frinak, H. Mao, R. W. Talbot, and B. C. Sive (2010), Temporal variability, sources, and sinks of C 1-C 5 alkyl nitrates in coastal New England, *Atmospheric Chemistry and Physics*, *10*, 1865–1883.

Sander, R. (2015), Compilation of Henry's law constants (version 4.0) for water as solvent, *Atmospheric Chemistry and Physics*, *15*(8), 4399–4981.

Schaefer, H., S. E. M. Fletcher, C. Veidt, K. R. Lassey, G. W. Brailsford, T. M. Bromley, E. J. Dlugokencky, S. E. Michel, J. B. Miller, I. Levin, D. C. Lowe, R. J. Martin, B. H. Vaughn, and J. W. C. White (2016), A 21st-century shift from fossil-fuel to biogenic methane emissions indicated by 13CH4, *Science*, *352*(6281), 80–84.

Shindell, D. T., M. Chin, F. Dentener, R. M. Doherty, G. Faluvegi, A. M. Fiore, P. Hess, D. M. Koch, I. A. MacKenzie, M. G. Sanderson, M. G. Schultz, M. Schulz, D. S. Stevenson, H. Teich, C. Textor, O. Wild, D. J. Bergmann, I. Bey, H. Bian, C. Cuvelier, B. N. Duncan, G. Folberth, L. W. Horowitz, J. Jonson, J. W. Kaminski, E. Marmer, R. Park, K. J. Pringle, S. Schroeder, S. Szopa, T. Takemura, G. Zeng, T. J. Keating, and A. Zuber (2008), A multi-model as-

sessment of pollution transport to the Arctic, *Atmospheric Chemistry and Physics*, *8*(17), 5353–5372.

Simon, H., L. Beck, P. V. Bhave, F. Divita, Y. Hsu, D. Luecken, J. D. Mobley, G. A. Pouliot, A. Reff, G. Sarwar, and M. Strum (2010), The development and uses of EPA's SPECIATE database, *Atmospheric Pollution Research*, *1*(4), 196–206.

Simpson, I. J., S. Meinardi, D. R. Blake, N. J. Blake, F. S. Rowland, E. Atlas, and F. Flocke (2002), A biomass burning source of C1-C4 alkyl nitrates, *Geophysical Research Letters*, *29*(24), 2168.

Simpson, I. J., S. K. Akagi, B. Barletta, N. J. Blake, Y. Choi, G. S. Diskin, A. Fried, H. E. Fuelberg, S. Meinardi, F. S. Rowland, S. A. Vay, A. J. Weinheimer, P. O. Wennberg, P. Wiebring, A. Wisthaler, M. Yang, R. J. Yokelson, and D. R. Blake (2011), Boreal forest fire emissions in fresh Canadian smoke plumes: C1-C10 volatile organic compounds (VOCs), CO2, CO, NO2, NO, HCN and CH3CN, *Atmospheric Chemistry and Physics*, *11*(13), 6445–6463.

Simpson, I. J., M. P. Sulbaek Andersen, S. Meinardi, L. Bruhwiler, N. J. Blake, D. Helmig, F. S. Rowland, and D. R. Blake (2012), Long-term decline of global atmospheric ethane concentrations and implications for methane, *Nature*, *488*(7412), 490–494.

Singh, H. B. (1987), Reactive nitrogen in the troposphere, *Environmental Science & Technology*, *21*(4), 320–327.

Talbot, R. W., J. E. Dibb, E. M. Scheuer, J. D. Bradshaw, S. T. Sandholm, H. B. Singh, D. R. Blake, N. J. Blake, E. Atlas, and F. Flocke (2000), Tropospheric reactive odd nitrogen over the South Pacific in austral springtime, *Journal of Geophysical Research: Atmospheres*, *105*(D5), 6681–6694.

Talukdar, R. K., J. B. Burkholder, M. Hunter, M. K. Gilles, J. M. Roberts, and A. R. Ravishankara (1997), Atmospheric fate of several alkyl nitrates Part 2UV absorption cross-sections and photodissociation quantum yields, *Journal of the Chemical Society, Faraday Transactions*, *93*(16), 2797–2805.

Torres, A. L., and A. M. Thompson (1993), Nitric oxide in the equatorial Pacific boundary layer: SAGA 3 measurements, *Journal of Geophysical Research: Atmospheres (1984–2012)*, *98*(D9), 16,949–16,954.

Travis, K. R., D. J. Jacob, J. A. Fisher, P. S. Kim, E. A. Marais, L. Zhu, K. Yu, C. C. Miller, R. M. Yantosca, M. P. Sulprizio, A. M. Thompson, P. O. Wennberg,

J. D. Crounse, J. M. St Clair, R. C. Cohen, J. L. Laughner, J. E. Dibb, S. R. Hall, K. Ullmann, G. M. Wolfe, I. B. Pollack, J. Peischl, J. A. Neuman, X. Zhou, and Zhou (2016), Why do models overestimate surface ozone in the Southeast United States?, *Atmospheric Chemistry and Physics*, *16*(21), 13,561–13,577.

Turner, A. J., D. J. Jacob, K. J. Wecht, J. D. Maasakkers, E. Lundgren, A. E. Andrews, S. C. Biraud, H. Boesch, K. W. Bowman, N. M. Deutscher, M. K. Dubey, D. W. T. Griffith, F. Hase, A. Kuze, J. Notholt, H. Ohyama, R. Parker, V. H. Payne, R. Sussmann, C. Sweeney, V. A. Velazco, T. Warneke, P. O. Wennberg, and D. Wunch (2015), Estimating global and North American methane emissions with high spatial resolution using GOSAT satellite data, *Atmospheric Chemistry and Physics*, *15*(12), 7049–7069.

Turnock, S., O. Wild, F. Dentener, Y. Davila, L. Emmons, J. Flemming, G. Folberth, D. Henze, J. Jonson, T. Keating, S. Kengo, M. Lin, M. Lund, S. Tilmes, and F. O amp apos Connor (2018), The Impact of Future Emission Policies on Tropospheric Ozone using a Parameterised Approach, *Atmospheric Chemistry and Physics Discussions*, pp. 1–41.

Tzompa-Sosa, Z. A., E. Mahieu, B. Franco, C. A. Keller, A. J. Turner, D. Helmig, A. Fried, D. Richter, P. Weibring, J. Walega, T. I. Yacovitch, S. C. Herndon, D. R. Blake, F. Hase, J. W. Hannigan, S. Conway, K. Strong, M. Schneider, and E. V. Fischer (2017), Revisiting global fossil fuel and biofuel emissions of ethane, *Journal of Geophysical Research: Atmospheres*, *122*(4), 2493–2512.

Vestreng, V., and H. Klein (2002), Emission data reported to UNECE/EMEP: Quality assurance and trend analysis & presentation of WebDab, *Tech. Rep. EMEP/MSC-W NOTE 1/2002*, Oslo, Norway.

Walker, T. W., R. V. Martin, A. van Donkelaar, W. R. Leaitch, A. M. MacDonald, K. G. Anlauf, R. C. Cohen, T. H. Bertram, L. G. Huey, M. A. Avery, A. J. Weinheimer, F. M. Flocke, D. W. Tarasick, A. M. Thompson, D. G. Streets, and X. Liu (2010), Trans-Pacific transport of reactive nitrogen and ozone to Canada during spring, *Atmospheric Chemistry and Physics*, *10*(17), 8353–8372.

Wesely, M. L. (1989), Parameterization of surface resistances to gaseous dry deposition in regional-scale numerical models, *Atmospheric Environment (1967)*, *23*(6), 1293–1304.

Williams, J. E., G. Le Bras, A. Kukui, H. Ziereis, and C. A. M. Brenninkmeijer (2014), The impact of the chemical production of methyl nitrate from the NO + CH3O2 reaction on the global distributions of alkyl nitrates, nitrogen oxides and tropospheric ozone: a global modelling study, *Atmospheric Chemistry and Physics*, *14*(5), 2363–2382.

Wu, S., L. J. Mickley, D. J. Jacob, J. A. Logan, R. M. Yantosca, and D. Rind (2007), Why are there large differences between models in global budgets of tropospheric ozone?, *Journal of Geophysical Research*, *112*, D05,302.

Yarwood, G., S. Rao, M. Yocke, and G. Whitten (2005), *Updates to the carbon bond chemical mechanism: CB05*, Final report to the US EPA.

Zafiriou, O. C., and M. McFarland (1981), Nitric oxide from nitrite photolysis in the central equatorial Pacific, *Journal of Geophysical Research: Atmospheres (1984–2012)*, *86*(C4), 3173–3182.

Zhang, L., D. J. Jacob, K. F. Boersma, D. A. Jaffe, J. R. Olson, K. W. Bowman, J. R. Worden, A. M. Thompson, M. A. Avery, R. C. Cohen, J. E. Dibb, F. M. Flock, H. E. Fuelberg, L. G. Huey, W. W. McMillan, H. B. Singh, and A. J. Weinheimer (2008), Transpacific transport of ozone pollution and the effect of recent Asian emission increases on air quality in North America: an integrated analysis using satellite, aircraft, ozonesonde, and surface observations, *Atmospheric Chemistry and Physics*, *8*(20), 6117–6136.

Zhang, L., D. J. Jacob, X. Liu, J. A. Logan, K. Chance, A. Eldering, and B. R. Bojkov (2010), Intercomparison methods for satellite measurements of atmospheric composition: application to tropospheric ozone from TES and OMI, *Atmospheric Chemistry and Physics*, *10*(10), 4725–4739.

Zhang, Q., D. G. Streets, G. R. Carmichael, K. B. He, H. Huo, A. Kannari, Z. Klimont, I. S. Park, S. Reddy, J. S. Fu, D. Chen, L. Duan, Y. Lei, L. T. Wang, and Z. L. Yao (2009), Asian emissions in 2006 for the NASA INTEX-B mission, *Atmospheric Chemistry and Physics*, *9*(14), 5131–5153.